

1 Platinum-group element geochemistry of the volcanic rocks associated with the Jaguar and
2 Bentley Cu-Zn volcanogenic massive sulfide (VMS) deposits, Western Australia: Implications
3 for the role of chalcophile element fertility on VMS mineralization.

4

5 Jung-Woo Park^{1,2*} and Ian Campbell²

6 ¹ School of Earth and Environmental Sciences, Seoul National University, Seoul 08826, South
7 Korea

8 ² Research School of Earth Sciences, Australian National University, Canberra, ACT 2601,
9 Australia

10 * Corresponding author: jung-woo.park@snu.ac.kr

11

12 **Abstract**

13 We report whole-rock major, trace, and platinum-group element (PGE) geochemistry of
14 volcanic rocks from the Teutonic Bore complex that hosts the Jaguar and Bentley Cu-Zn
15 volcanogenic massive sulfide (VMS) deposits. This study aims to understand their sulfide
16 saturation history and chalcophile element evolution during differentiation of the Jaguar and
17 Bentley magmas, and investigate the role of chalcophile element fertility on the formation of
18 VMS deposits.

19 The fractionated primitive mantle-normalized trace element patterns, with negative Nb and
20 Ti anomalies of basalts, andesites, dacites and rhyolites from Jaguar and Bentley are similar to
21 each other. The trace elements and PGE show continuous variations when plotted against
22 fractionation indices such as Yb, which can be explained by a two-stage fractional
23 crystallization model: Stage 1 Rayleigh fractionation of plagioclase + clinopyroxene + Cr-
24 spinel, and Stage 2 the fractional of plagioclase + clinopyroxene + magnetite + 0.1 wt.% sulfide
25 liquid. Dolerites, which postdate the mineralization, differ from the other rock types and require
26 a different magma source.

27 Andesite and basalt are the most PGE-enriched lithologies in Jaguar and Bentley. The PGE
28 behave incompatibly in the early stage of magma differentiation at < 4 ppm Yb, whereas they
29 abruptly decrease at > 4 ppm Yb, indicating sulfide saturation at this point. When Pd/MgO and
30 Pd/Pt are used as chalcophile element fertility indicators, the andesite before sulfide saturation
31 (< 4 ppm Yb) is as fertile as the magmas associated with porphyry Cu-only deposits. In contrast,
32 the andesite after sulfide saturation and other lithologies are characterized by markedly
33 depleted fertility similar to those of barren suites. This suggests that sulfide-undersaturated
34 andesite, and probably basalt, may have been a significant source for Cu in the Jaguar and
35 Bentley Cu-Zn VMS deposits. However, the Au fertility of the Jaguar and Bentley andesite

36 must have been low and not enough to form Au-rich VMS deposits because their Pd/MgO and
37 Pd/Pt values are 5-10 times lower than those of andesite and dacite from the modern Au-rich
38 seafloor massive sulfide deposits. This can be explained if ore formation occurred shortly after
39 sulfide saturation. If the amount of sulfide melt to precipitate was small, Au, with its high
40 partition coefficient into immiscible sulfide melts, would have been largely stripped from the
41 silicate melt whereas Cu, with its lower partition coefficient, would be little affected. Our study
42 shows that chalcophile element fertility may play an important role in the formation of VMS
43 deposits, especially in controlling the Au contents of the ore, if the magmatic-hydrothermal
44 component is the dominant source for metals in VMS systems.

45 **Introduction**

46 There are two principal hypotheses for the source of the metals in volcanogenic massive
47 sulfide (VMS) deposits, the wall rock leaching, and magmatic-hydrothermal hypotheses. In the
48 former, the metals are leached from the wall rocks above a sub-volcanic magma chamber,
49 which drives convection in the overlying volcanic rocks. The latter requires them to be
50 deposited from a magmatic fluid, derived from an underlying magma chamber (Campbell et
51 al., 1981; Franklin et al., 2005; Yang and Scott, 1996; Huston et al., 2011; de Ronde et al. 2011;
52 Patten et al., 2020). Both sources may contribute to the formation of VMS deposits, although
53 their relative contributions may vary.

54 Studies of seafloor massive sulfide (SMS) deposits, the modern equivalent of VMS systems,
55 provide critical information as to the source of metals and S in VMS systems. The presence of
56 advanced argillic alteration and native sulfur with negative $\delta^{34}\text{S}$ values in some arc-related
57 SMS deposits require the input of a magmatic component into the ore-forming hydrothermal
58 fluid (Huston et al., 2011). The arc-associated SMS deposits discharge vent fluids with
59 significantly higher magmatic volatile and metal contents such as SO_2 , H_2S , CO_2 and Fe than
60 those at mid-ocean ridge (MOR) settings (de Ronde et al., 2001, 2011, 2014; Massoth et al.,
61 2003; Lupton et al., 2006, 2008; Resing et al., 2007, 2009; Butterfield et al., 2011). It has been
62 suggested that these volatiles are responsible for transporting economic metals such as Au and
63 Cu from the sub-volcanic magma chambers to the SMS systems (de Ronde et al., 2005, 2011,
64 2014; Berkenbosch et al., 2012; Gruen et al., 2014). These observations, together with the
65 higher concentrations of Au, As, Sb, and Hg in sulfides from some arc-related SMS deposits
66 compared with those associated with MOR, suggest higher magmatic input into the former. A
67 recent mass balance study (Patten et al., 2020) on Izu-Bonin arc oceanic crust, and associated
68 VMS mineralization, showed that leaching alone could not explain the enrichment of Se, S,

69 and Au in the mineralized samples and significant metal fluxes from magmatic-hydrothermal
70 fluids are necessary.

71 The Teutonic Bore complex of Western Australia hosts three Archean Cu-Zn VMS deposits:
72 the Teutonic Bore, Jaguar and Bentley, over a distance of about 8 km (Fig. 1; Belford, 2010).
73 The steeply dipping banded massive sulfide layers are hosted by a sequence of pillow basalt
74 with intercalated dacite breccias and sedimentary rocks (Hallberg and Thomson, 1985; Belford,
75 2010; Belford et al., 2015). Multi-sulfur isotope studies for the Teutonic Bore, Jaguar and
76 Bentley deposits (Chen et al., 2015) have shown that the $\Delta^{33}\text{S}$ of the ores is slightly negative
77 from -0.46 to -0.05 ‰, in contrast to pyrites from wall rocks, which include sedimentary rocks
78 that range from $+0.19$ to $+6.20$ ‰. Chen et al. (2015), based on the S isotope results, argued
79 that the ore S is a mixture of magmatic and seawater S, dominated by the former with a
80 negligible contribution from the country rocks. Given that S is the major anion in the VMS ore
81 and the major component of the ligands, together with Cl, which transport Cu and Au in the
82 ore-forming fluids (Huston, 1997), it is likely that Cu and Au in the ores from the Teutonic
83 Bore, Jaguar and Bentley deposits were mainly derived from an underlying magma body.

84 If the above argument is correct, the Cu and Au ore potential of the volcanic package is likely
85 to be mostly dependent on the nature of the fractionation process in the underlying magma
86 chamber, and especially on the timing of sulfide saturation relative to volatile saturation in the
87 evolving melt (Park et al., 2013; 2015; 2019). Early sulfide saturation leads to depletion of the
88 chalcophile elements, which include Cu and Au, so that they are unavailable to enter the
89 magmatic-hydrothermal fluid when the magma becomes volatile saturated (Cocker et al., 2015;
90 Park et al., 2019). Alternatively, if sulfide saturation occurs late, after or shortly before volatile
91 saturation, the chalcophile elements are concentrated by fractional crystallization and are
92 available to enter the fluid phase when the magma eventually become fluid-saturated (Park et

93 al., 2019). Note that the effect of sulfide segregation will be limited for Zn and Pb due to their
94 affinity for sulfide phases being weaker than Cu and Au.

95 Platinum-group element (PGE) have been used to test the hypothesis that the time of sulfide
96 saturation, relative to volatile saturation, controls the fertility of porphyry Cu and porphyry Cu-
97 Au deposits (Cocker et al., 2015; Park et al., 2019; Hao et al. 2017; 2019; Lowczak et al., 2018).
98 The PGEs are preferred for two reasons, first because their partition coefficients into an
99 immiscible sulfide melt are at least two orders of magnitude higher than Cu, and an order of
100 magnitude higher than Au (Mungall and Brenan, 2014); and second because the PGEs are less
101 mobile than Cu and Au in seafloor hydrothermal settings (Crocket et al., 2000; Park et al.,
102 2016).

103 In this study, we report the results of major and trace element analyses, including PGEs, in
104 volcanic rocks from the Jaguar and Bentley Cu-Zn VMS deposits using a NiS fire assay-isotope
105 dilution method, which has a detection limit of 15 ppt (part per trillion) for Pt and Pd, and ca.
106 1 ppt for the other PGE. The aim was to determine the point at which the evolving magma
107 systems, which produced the Jaguar and Bentley VMS deposits, reached sulfide saturation, and
108 to ascertain its influence on the evolution of the chalcophile elements. We also discuss the role
109 of chalcophile element fertility on Cu and Au mineralization in VMS ore deposits by
110 comparing PGE data of volcanic rocks that host the Jaguar and Bentley Cu-Zn VMS deposits
111 with those of the Pual Ridge and Niuatahi Au-rich SMS deposits.

112

113 **Geological setting**

114 The Teutonic Bore, Jaguar and Bentley VMS deposits are located in the Teutonic Bore
115 volcanic complex in the northern Gindalbie Domain of the Kurnalpi terrane, Eastern Goldfields

116 Superterrane (EGST), Western Australia (Belford et al., 2015). The Archean EGST is
117 composed of deformed and metamorphosed volcanic and sedimentary rocks, which were later
118 intruded by granite batholiths (Barley et al., 2008). The volcanic and sedimentary rocks were
119 deposited between ~2930 and ~2650 Ma and underwent low to medium grade greenschist
120 facies metamorphism (Swager et al., 1992; Cassidy et al., 2002). Late granitoids, with ages
121 from 2680 to 2660 Ma, intruded into the greenstone belts (Cassidy et al., 2002), which were
122 subjected to major N-S to NNE-SSW trending faulting (Swager, 1997).

123 The Gindalbie Domain hosts four major volcanic complexes: Melita, Teutonic Bore, Spring
124 Well, and Jeedamyia. They range in age from 2694 ± 4 Ma to 2676 ± 5 Ma (Nelson, 1995;
125 Nelson, 1997a; Nelson, 1997b; Brown et al., 2002; Kositcin et al., 2008). The Melita and
126 Teutonic Bore complexes are characterized by high field strength element (HFSE) enriched
127 bimodal volcanism, whereas the Spring Well and Jeedamyia complexes consist of calc-alkaline
128 intermediate and silicic volcanic rocks (Barley et al., 2008). The role of subduction in the
129 petrogenesis of the volcanic rocks is contentious. Belford et al. (2015) invoked a back-arc
130 setting for the Gindalbie Domain adjacent to the Teutonic Bore; however, Barnes and Van
131 Kranendonk (2014) suggested that plume-related magmatism accompanied by magma mixing
132 and crustal assimilation can explain the geochemistry of felsic and intermediate volcanic rocks
133 in the Eastern Goldfields superterrane. Regardless of whether or not subduction is required,
134 young Nd_{DM} ages and juvenile Pb isotope signatures, compared to those of the surrounding
135 volcanic units, indicates that the VMS mineralization occurred along rift margins such as a
136 continental-rift or back-arc basin rift system (Huston et al., 2014; Hollis et al., 2015).

137 The Teutonic Bore complex hosts the Teutonic Bore, Jaguar, and Bentley VMS deposits (Fig.
138 1). Hallberg and Thompson (1985) investigated the geologic setting of the Teutonic Bore
139 deposit, and a summary of their study follows. The oldest exposed rocks are amygdaloidal

140 andesites that are overlain first by pillowed basalts, and then by rhyolitic volcanic and
141 volcanoclastic rocks. The felsic rocks are, in turn, overlain by a second sequence of pillowed
142 basalts that host most of the mineralization. The basalts are interspersed with polymict
143 conglomerate and greywacke layers or lenses. The massive sulfide ore body occurs 0 and 150
144 m stratigraphically above the boundary between the rhyolite and basalt. Dolerite sills and dykes
145 intrude all of the volcanic units. Nelson (1997b) reported a SHRIMP zircon U-Pb age of 2692
146 ± 4 Ma for a hanging-wall porphyritic dacite from the Teutonic Bore. Hayman et al. (2014)
147 reported thermal ionization mass spectrometry (TIMS) zircon U-Pb ages of 2692.6 ± 1.5 Ma
148 and 2694.2 ± 0.6 Ma for a hanging-wall rhyolite dyke (Jaguar) and the footwall rhyolite
149 (Bentley), respectively.

150 Belford (2010) and Belford et al. (2015) studied the stratigraphy, geochemistry, and
151 petrology of the host successions of the Jaguar VMS deposit. The following is a summary of
152 Belford et al. (2015). The oldest unit of the Jaguar deposit is massive coherent andesite with
153 thickness > 50 m. Its lower contact is not exposed. The andesite unit is intruded by a rhyolite
154 dome, which is overlain by andesite that erupted on the seafloor. Basalt conformably overlies
155 the andesite with no interflow sediment separating the units. Sedimentary facies are rare in the
156 footwall of the Jaguar deposit, suggesting a high rate of volcanic accumulation and that
157 volcanic hiatus are short or absent. The basalt is overlain by a laminated chert and pumice rich
158 facies, which in turn is overlain by coherent and polymict dacites forming a series of small
159 domes that were extruded onto the seafloor. The Jaguar massive sulfide body is hosted by the
160 coherent dacites and their associated volcanoclastic rocks, which together are classified as the
161 mineralized package by Belford et al. (2015). Later dolerite dykes crosscut all of the facies
162 described above.

163

164 **Samples**

165 The coherent volcanic rocks analyzed for this study were collected from four drill holes:
166 13JUDD002, 12JADD002, 09BTDD029, and 09BTDD025 (Electronic Supplementary
167 Material (ESM) Table 1; Fig. 2). These holes cover most of the coherent volcanic lithofacies
168 that hosts the Jaguar and Bentley deposits. The samples are fresh to the extent that they still
169 preserve primary igneous textures despite prevalent regional greenschist facies metamorphism
170 and local hydrothermal alteration. The igneous rock classification of the Jaguar and Teutonic
171 Bore areas has been performed using HFSE, which are immobile during greenschist
172 metamorphism (Hallberg and Thompson, 1984; Belford et al., 2015). In this study, we used
173 Ti/Zr to classify the major igneous rock types. The Ti/Zr criteria are: rhyolite < 4 < dacites $<$
174 12 < andesite < 50 < basalt (Hallberg, 1984). Note that Ti/Zr = 50, instead of 60 as suggested
175 in Hallberg (1984), has been used to discriminate between andesite and basalt. Y/Zr was also
176 used as an index to classify the rocks as tholeiite ($2 < Y/Zr < 4.5$), transitional ($4.5 < Y/Zr < 7$),
177 or calc-alkaline ($7 < Y/Zr < 25$) (MacLean and Barrett, 1993).

178 Drill hole 13JUDD002 is an underground hole that was drilled from the same level as the
179 mineralized package toward the stratigraphic footwall. It cuts andesite, basalt, and dolerite,
180 which are considered to be part of the footwall, but distal to the mineralized and footwall
181 rhyolites. The dolerite shows sharp upper and lower contacts with andesite and basalt, with
182 well-developed chilled margins. This suggests late intrusion of dolerite into the andesite and
183 basalt sequences in the mineralized package. The basalts are interspersed with layers of wacke,
184 chert, and siltstone from 40 to 70 m. Between 400 m and 430 m, where they are close to the
185 footwall rhyolite, they are partly brecciated and intercalated with feldspathic and quartz phyric
186 rhyolite. Weak pyrite and chalcopyrite veining occurs in the brecciated basalt-rhyolite zone.
187 The footwall rhyolite is silicified and has experienced sericitization and chloritization. A total

188 of twenty-two samples were collected from this core, consisting of two andesites from the
189 mineralized package and two andesites, six basalts, and five rhyolite samples from footwall
190 and seven dolerite samples.

191 Drill hole 12JADD002 is one of the three northernmost holes designed to investigate the
192 lithology of the northeastern Jaguar area. It cuts through the hanging-wall basalt, andesite and
193 rhyolite, and the footwall basalt and rhyolite as well as dolerite. The rocks between 212 m and
194 480 m are weakly deformed and sheared. At 310 m, the host rock is partially replaced by 30%
195 pyrite, which is interpreted to be the distal end of the main Jaguar ore body. A total of twenty
196 samples were collected from this hole. They include four basalts, two rhyolites and one andesite
197 from the hanging-wall sequence, together with three basalts and four rhyolite samples from the
198 footwall sequence, and four dolerite samples.

199 Drill hole 09BTDD029 was drilled through the hanging-wall, the mineralized package
200 lithofacies, and footwall rhyolite of the Bentley deposit. The hanging-wall volcanic facies from
201 this hole consists mainly of andesite. A total of thirteen samples consisting of nine hanging-
202 wall andesite-, two foot-wall rhyolites, and five dolerites were collected from this hole.

203 Drill hole 09BTDD025 crosses from the hanging-wall lithofacies through the main massive
204 Cu-Zn sulfide ore body into the footwall rhyolite. The hanging-wall volcanic facies consist of
205 basalt, andesite, and rhyolite. A total of twenty-three samples were collected, consisting of five
206 andesites, three basalts, and three rhyolites from the hanging-wall sequence along with five
207 footwall rhyolite and four massive and stringer ore samples.

208 Six additional footwall volcanic and intrusive rocks from the Bentley deposit were collected
209 from drill holes 12TRDD016, 13TRDD009, 09TRDD032, and 13TRDD001, which include
210 three andesites, one dacite, and two dolerite samples. One footwall rhyolite was also collected

211 from drill hole 13TRDD014 from the Teutonic Bore deposit.

212 Coherent volcanic rocks, with small amounts of phenocrysts (<~10 modal %), were used in
213 this study. The rhyolite is composed of a fine-grained matrix with quartz phenocrysts (< 1-2
214 mm). The matrix minerals are dominantly quartz, sericite, and chlorite and show varying
215 degree of silicification. The andesite is amygdaloidal and aphyric to feldspar-phyric. The round
216 and elongated amygdales (~1-3 mm) are filled with quartz or carbonate minerals. Overall the
217 size of plagioclase laths varies from 1 to 3 mm. In some cases, the plagioclase phenocrysts and
218 microcrystalline matrix are replaced with sericite, carbonate, and chlorites. Basalt is
219 dominantly aphyric. Microtextures vary from sub-ophitic texture with plagioclase laths and
220 pyroxene to intersertal with plagioclase and microrites.

221

222 **Analytical techniques**

223 Major element analysis

224 The major element compositions of twenty-three samples were measured by X-ray
225 fluorescence (XRF) analysis at Genalysis Laboratories in Perth, Western Australia, using the
226 whole-rock lithium borate fusion XRF package FB1/XRF20. The results are reported in Table
227 1. A further thirty-two samples, including seventeen of the samples that had been analyzed by
228 XRF, were selected for whole rock analysis by electron microprobe. The samples were crushed
229 in a steel jaw crusher and milled in a tungsten carbide mill at the Australian National University
230 (ANU). About 0.5 g of each sample powder was fused in a graphite crucible in an open furnace
231 at 1400 °C for 1 hour and quenched in tap water. The quenched glass was mounted on an
232 epoxy disk, and the major element compositions were measured by Cameca SX100 microprobe
233 at ANU with an accelerating voltage of 15 KeV, beam current of 10 nA and beam diameter of

234 10 μm . The results are reported in ESM Table 2. The probe data differ from the XRF data by
235 more than 10% for some samples, particularly in FeO, MnO, Na₂O, and P₂O₅. The discrepancy
236 is attributed to incomplete fusion in the absence of the Li-borate flux, a conclusion supported
237 by patches of microcrystals in glass chips of some felsic samples. Systematically low
238 microprobe FeO data can be attributed to the formation of Fe metal phases during fusion, which
239 results in depletion of FeO in a silicate melt. However, SiO₂ contents measured by the two
240 methods vary by less than 10 % (ESM Fig. 1). The SiO₂ contents were used to calculate trace
241 element concentrations of the samples during LA-ICP-MS data reduction.

242

243 Trace element analysis by LA-ICP-MS

244 A total of twenty-nine samples were analyzed for trace elements by LA-ICP-MS at ANU.
245 The sample powder (~0.6 g) was mixed with Li-borate flux with a sample/flux ratio of 1/3. The
246 mixture was dried at 400 °C for 10 min, fused at 1050 °C for 8 min and then poured onto a
247 graphite mold to make a glass disk. The laser system consists of a Lambda Physik Complex
248 110 excimer laser ($\lambda = 193 \text{ nm}$) and ANU-designed HelEx cell combined with an Agilent 7700x
249 ICP-MS. The analyses were performed at the laser pulse rate of 5 Hz, beam size of 81 μm , and
250 energy density of ~ 3 J/cm². NIST 610 glass was used as the external standard for calculating
251 the trace element concentrations with reference to the Si content of the glass as determined
252 either by XRF or electron microprobe. Averages of three to five analyses of each sample are
253 reported in Table 2. Seven analyses of the USGS reference material BCR-2g were carried out
254 along with unknown samples in order to check the reproducibility and precision of the analyses.
255 The measured BCR-2g values agree well with those reported by Jochum et al. (2008) within
256 the quoted uncertainties. The percentage relative difference (%RD) is less than 6% for all
257 elements except for Cr (15 %), Ni (11 %), Cu (16 %) and Zn (25 %). The reproducibility,

258 calculated as relative standard deviation (1σ) based on counting statistics, was mostly less than
259 4 % (Table 2).

260

261 Platinum-group element and Re analysis by a Ni-sulfide fire assay and isotope dilution method

262 Twenty-three samples were analyzed for PGE and Re following the method described by
263 Park et al. (2012). Briefly, 5 g sample powder was mixed with Ni, S, and sodium borax powder
264 (sample: Ni : S : sodium borate = 10 : 1 : 2: 10) on a weighing paper, and the mixture was
265 poured into a porcelain CoorsTM crucible. The PGE spikes (⁹⁹Ru, ¹⁰⁵Pd, ¹⁸⁵Re, ¹⁹¹Ir, and ¹⁹⁵Pt)
266 were added to the mixture. The crucible containing the mixture and spike was then placed into
267 the second crucible containing 0.1 g of flour and covered by a porcelain lid. The sample mixture
268 was dried at 100 °C for 60 min, fused at 1100 °C for 30 min, and quenched in the air by
269 removing the crucible from the furnace. During fusion, N₂ gas was introduced at a flow rate of
270 ~0.03 m³/min. After quenching, Ni-sulfide beads containing the PGE were collected and
271 dissolved in 150 ml of 6 N HCl, and the solution was filtered through a Millipore filter paper.
272 The filter was digested in 4 ml of aqua regia. After the complete digestion of the filter paper,
273 the solution was dried to ~100 µl and diluted with 2 % nitric acid. The final solution was
274 analyzed by an Agilent 7700x ICP-MS at ANU. The sensitivities were ~2–3 × 10⁵ cps per
275 ppb for mass 89, 140, and 205. Argide and oxide production rates were measured using pure
276 solutions of Ni, Cu, Zn, Co, Hf, Mo, and Zr to correct molecular isobaric interferences on the
277 PGE. The argide production rate ranges from 0.002% to 0.004% and oxide rate from 0.2% to
278 0.6%. The molecular interferences on all PGE were < 0.1% except Ru for which the Ni argide
279 interference was < 30 % for all samples but JB44605 where the interference was 68 %. This is
280 largely due to the Ru content of JB44605 being close to the limit of detection. Concentrations
281 of Pd, Pt, Ir, Ru, and Re were determined by isotope dilution method using the ¹⁰⁵Pd/¹⁰⁸Pd,

282 $^{195}\text{Pt}/^{194}\text{Pt}$, $^{191}\text{Ir}/^{193}\text{Ir}$, $^{99}\text{Ru}/^{101}\text{Ru}$, and $^{185}\text{Re}/^{187}\text{Re}$, respectively. Rhodium concentrations were
283 calculated using the method described in Park et al. (2012).

284 Average procedural blanks determined from four analyses using 10 g of sodium borax, 1 g
285 of Ni and 0.5 g of S were 0.9 ± 0.1 ppt for Ir, 1.9 ± 0.4 for Ru, 0.9 ± 0.1 ppt for Rh, 7.5 ± 1.8
286 ppt for Pt, 14 ± 3.3 ppt for Pd and 21 ± 4.0 ppt for Re. The blank corrected PGE data are
287 reported in Table 3. The method detection limits (MDL), taken to be two standard deviations
288 of the procedural blanks, were 0.2 ppt Ir, 1 ppt Ru, 0.3 ppt Rh, 4 ppt Pt, 8 ppt Pd, and 8 ppt Re.
289 The uncertainties (1σ) arising from ICP-MS counting statistics, the PGE calibration standard,
290 and blank subtraction are given. Multiple analyses of the CANMET TDB-1 reference material
291 were performed to test the accuracy and precision of the measurements (Table 3). The results
292 agree well with the values previously reported by Meisel and Moser (2004), and Peucker-
293 Ehrenbrink et al. (2003).

294

295 **Results**

296 Major and trace element

297 Although the samples were selected on a least-altered basis, the major element geochemistry
298 of Jaguar and Bentley volcanic rocks has, to some extent, been affected by hydrothermal
299 alteration and greenschist facies metamorphism. Selected major elements are plotted against
300 SiO_2 in ESM Fig. 2. Al_2O_3 , CaO show negative correlations with SiO_2 , suggesting they may
301 represent magmatic trends. However, MgO, FeO, K_2O , and Na_2O data are scattered, which can
302 be attributed to moderate hydrothermal alteration.

303 High field strength elements (Ti, Zr, Y, Nb, REE, Hf, Ta, and Th) and some transition metals
304 (V, Cr, Ni, and Co) are considered to be chemically immobile at moderate degrees of

305 hydrothermal alteration and greenschist facies metamorphism (Pearce and Cann, 1973;
306 Winchester and Floyd, 1977; Whitford et al., 1989; MacLean and Barrett, 1993). The samples
307 analyzed in this study are compared with the geochemical data of 243 core samples from the
308 Jaguar and 240 core samples from the Bentley in terms of the immobile elements in ESM Fig.
309 3. The samples from this study represent most of the rock types that occur in the two deposits,
310 except for the calc-alkaline andesite and the dacite (ESM Fig. 3). The calc-alkaline andesites
311 of the Jaguar deposit are found mostly in hanging-wall units, whereas footwall andesites have
312 transitional geochemical features with Zr/Y between 4.7 and 6.9 (Belford, 2010). Therefore,
313 the calc-alkaline andesites are unlikely to be associated with the mineralization at the Jaguar
314 and have therefore been omitted from this study. Dacite is a major rock type within the
315 mineralized package at the Jaguar and is thought to be a differentiation product of the footwall
316 andesites (Belford, 2010). However, they only account for a small volume of the volcanic
317 successions in the Jaguar suite (Belford, 2010).

318 In Figure 3, the immobile trace element concentrations of the Teutonic Bore, Jaguar and
319 Bentley volcanic rocks are normalized to primitive mantle values (McDonough and Sun, 1995).
320 The patterns of volcanic rocks from three deposits are similar (Fig. 3). The basalt, andesite,
321 dacite, and rhyolites show similar fractionated patterns with marked negative Nb and Ti
322 anomalies (Fig. 3). The negative Ti anomalies become more pronounced with increasing Yb
323 contents (i.e., increasing fractionation) in the andesite, dacite, and rhyolite (Fig. 3a and b). The
324 trace element patterns of the andesite and rhyolite closely match those of Phanerozoic calc-
325 alkaline island arc andesite and rhyolite, respectively (Fig. 3a and b). The dolerite is distinct
326 from the other rock types, having flat trace element patterns with appreciably smaller negative
327 Nb and Ti anomalies (Fig. 3d).

328 Figure 4 compares the chondrite-normalized REE patterns of the Teutonic Bore, Jaguar, and

329 Bentley volcanic rocks analyzed for this study with Belford (2010). Belford (2010) documented
330 the geochemical features and the geometry of the volcanic rocks that host the Jaguar deposit
331 by logging of 24 km of drill core. The REE patterns of rhyolites from the Teutonic Bore, Jaguar
332 and Bentley are slightly to moderately fractionated with $La_N/Yb_N = 3.9$ to 5.8 , and marked
333 negative Eu anomalies (Fig. 4a). There is no systematic variation among the three localities.
334 Their patterns are similar to the dacites from the mineralized package from the Jaguar deposit
335 (Belford, 2010), which are considered to be less fractionated rhyolites.

336 The andesites from the mineralized package of the Jaguar deposit, analyzed for this study,
337 are moderately fractionated with La_N/Yb_N ranging from 5.5 to 5.6 and small Eu anomaly (Fig.
338 4b). This trend differs from the patterns of typical footwall andesites from the Jaguar deposit
339 (Belford, 2010), but is similar to the hanging-wall andesite (Fig. 4b). The andesites from both
340 the hanging-wall and footwall of the Bentley deposit are characterized by slightly fractionated
341 REE patterns ($La_N/Yb_N = 3.3$ to 4.2) with small negative Eu anomalies (Fig. 4b). Their patterns
342 are nearly identical to the footwall andesites from the Jaguar deposit in Belford et al. (2015).

343 The REE patterns of the basalts from the Jaguar and Bentley deposits in this study are
344 consistent with those of the footwall basalts reported in Belford (2010), despite higher REE
345 concentrations. They are slightly fractionated ($La_N/Yb_N = 2.9$ to 3.6) and show both positive
346 and negative Eu anomalies (Fig. 4c). Belford et al. (2015) attributed the positive Eu anomaly
347 shown in some of the basalts to the inclusion of cumulative plagioclase. The REE compositions
348 of dolerites are consistent in both the Jaguar and Bentley. They are characterized by flat REE
349 patterns ($La_N/Yb_N = 1.1$ to 1.6) with variable Eu anomalies (Fig. 4d).

350 Winchester and Floyd (1977) and Hallberg (1984) suggested Zr/TiO_2 and Ti/Zr as
351 fractionation indices for altered or metamorphosed volcanic rocks. However, the compatibility
352 of Ti and Zr can vary significantly during magma differentiation due to the crystallization of

353 Ti-bearing magnetite and zircon. Therefore, we use Yb as an index of fractional crystallization
354 in this study (e.g., Park et al., 2013). Ytterbium shows a clear positive correlation with other
355 immobile incompatible elements such as La, Y, Zr, and Nb (Fig. 5a and b; Table 2), and its
356 concentration increases through the overall fractionation sequence of basalt, andesite to
357 rhyolite. Note that basalt and andesite cannot be clearly distinguished by petrography due to
358 alteration, and classification of rock type is based on Ti/Zr ratios. Some basalt samples, with
359 Yb contents higher than andesite, may be misclassified probably due to local zircon saturation
360 or zircon inheritance from basement rocks (e.g., Hollis et al., 2015). They also contain very
361 low Cr (< 5 ppm) and Ni (< 11 ppm), suggesting they are the product of substantial magma
362 differentiation. Basalt and andesite form a continuum in most immobile trace element
363 variations (Fig. 5). Therefore, we will consider them as a single unit (basalt-andesite) in the
364 following discussion. Two andesite samples (JB44663 and JB44665) from the mineralized
365 package of the Jaguar deposit are slightly out of trend with higher La, Zr, and Nb than other
366 andesites at a given Yb, suggesting that they may be derived from a different parental magma
367 source or have undergone different evolutionary processes. The La and Zr contents of the
368 dolerites are significantly lower than those of other rock types over the same range of Yb (Fig.
369 5), implying that the dolerite originated from a different source that was depleted in La and Zr.

370 Chromium and Ni behave as compatible elements. Progressive depletion of Cr and Ni with
371 increasing Yb in the Jaguar and Bentley volcanic rocks (Fig. 5c and d) suggests olivine and Cr-
372 bearing clinopyroxene or chromite crystallization in the early stage of magma differentiation
373 (FC1). Titanium and V concentrations generally increase with increasing Yb in dolerite,
374 whereas their concentrations in basalt-andesite reach their maximum when Yb reaches about 4
375 ppm then decrease in the more fractionated samples (Fig. 5e and g). These trends suggest the
376 onset of magnetite crystallization at 4 ppm Yb in basalt-andesite (FC2). Note that the

377 geochemistry of andesite sample JB44906 is discordant to the trend of the majority of the
378 andesites with depleted Cr, Ni, Ti, and V over the same range of Yb as other rock types,
379 suggesting a different magma evolution history or an alteration effect. Note that the samples
380 JB44906 has the highest AI values among andesites (Fig. 8).

381

382 Platinum group elements and Re

383 The platinum group element concentrations are mostly below the method of determination
384 limit (m.d.l.) for rhyolites. Sample JB44699 is the least differentiated of the analyzed rhyolites
385 (i.e., the lowest Yb contents). It contains 0.333 ppb Pt, 0.001 ppb Rh and 0.005 ppb Ir, but the
386 other PGE concentrations, including Pd, are below the detection limits (Table 5). The PGE
387 concentrations in the basalt-andesite vary significantly between the samples with < 4 ppm Yb
388 and > 4 ppm Yb (Fig. 6). The basalt-andesite containing Yb < 4 ppm is enriched in PGE relative
389 to the latter. They contain 0.083 to 1.25 ppb Pd, 0.48 to 0.80 ppb Pt, 0.014 to 0.065 ppb Rh,
390 0.014 to 0.046 ppb Ru, and 0.008 to 0.014 ppb Ir. The PGE concentrations increase with
391 increasing Yb values in general, except for Ru, which shows a slight negative correlation with
392 Yb. Note that the basalt sample (JB44907) with Yb < 4 ppm contains PGE contents lower than
393 other basalt-andesite samples. It may have experienced some localized sulfide segregation.
394 Significantly lower PGE contents characterize the PGE contents in the most evolved basalt-
395 andesite (> 4 ppb Yb). The dolerites have the highest, but variable, PGE concentration among
396 all the rock types in the Jaguar and Bentley deposits. They contain < 0.008 to 5.03 ppb Pd, <
397 0.004 to 8.27 ppb Pt, < 0.0003 to 0.310 ppb Rh, < 0.001 to 0.028 Ru and < 0.0002 to 0.101 ppb
398 Ir. The PGE contents of the dolerite decrease with increasing Yb.

399 Copper contents of all the rock types show no clear trend with increasing Yb (Fig. 6f) and,

400 in this respect, differ from PGE. We attribute this difference to gain and loss of Cu during the
401 hydrothermal alteration associated with the mineralization as a consequence of the higher
402 mobility of Cu compared with the PGE in hydrothermal fluids (Crocket et al., 2000; Park et al.,
403 2016). There is no clear correlation between Cu and Pd. Rhenium concentrations range from
404 0.071 to 1.11 ppb in basalt-andesite, and 0.003 to 0.012 ppb in rhyolites. The dolerites have
405 high Re contents of 1.10 to 1.76 ppb.

406 Primitive mantle normalized PGE patterns of the Jaguar and Bentley volcanic rocks are
407 shown in Fig. 7. The basalt-andesite with > 4 ppb Yb is characterized by highly fractionated
408 patterns with a high Pd/Ir ratio ranging from 76 to 105, except for the basalt sample (JB44907).
409 These patterns are similar to those of the modern arc andesite, and their concentrations are at
410 the high end of the arc andesite range (Fig. 7a). The basalt-andesite with < 4 ppb Yb shows
411 similar PGE patterns but is substantially depleted in PGE concentrations. Two samples display
412 slightly negative Pd anomalies. The patterns of the Jaguar and Bentley basalt-andesite are
413 consistent with each other, which corresponds to their similar trace element geochemistry. One
414 rhyolite sample (JB44699) is enriched in Pt, Ir, and Rh compared to other rhyolites. The PGE
415 patterns of dolerite differ from those of the andesites. They are less fractionated with Pd/Ir
416 ranging from 38 to 50, and they have negative Ru anomalies. Although the absolute PGE
417 concentrations of three dolerite samples vary by more than an order of magnitude, the patterns
418 are sub-parallel to each other, indicating the same compatibility for all of the PGE (Fig. 7b).

419

420 **Discussion**

421 Effect of alteration

422 The whole-rock geochemistry of volcanic rocks associated with VMS deposits is often

423 affected by hydrothermal alteration. Large et al. (2001) proposed a graphical representation of
424 whole-rock geochemistry data, the alteration box plot, that provides information on alteration
425 mineralogy, and degree and type of alteration of the volcanic rocks. Most of the samples used
426 in this study plot within or close to the field of least altered volcanic rocks (Fig. 8), which
427 suggest they are likely to preserve magmatic compositions. Two exceptions are footwall
428 rhyolite samples of Jaguar and Bentley (Samples JB44681 and JB44922) that have an alteration
429 index larger than 80. They may have undergone intense chloritization and sericitization during
430 footwall alteration. Dolerite samples are characterized by a high CCP index (chlorite-
431 carbonate-pyrite; $100 \times (\text{MgO} + \text{FeO}) / (\text{MgO} + \text{FeO} + \text{Na}_2\text{O} + \text{K}_2\text{O})$) of $> \sim 80$. This may be
432 due to their primitive nature (e.g., high MgO contents) because the CCP index is affected by
433 magma differentiation and tends to decrease with decreasing MgO (Large et al., 2001).

434

435 Magma differentiation

436 The coherent volcanic rocks from the Jaguar and Bentley are composed of basalt, andesite,
437 dacite, and rhyolite (This study; Belford, 2010). Belford et al. (2015) reported that the footwall
438 volcanic rocks in the Jaguar deposit, which include basalt, andesite, dacite, and rhyolite, have
439 similarities in geochemistry and suggested that they originated from a common source. The
440 geochemistry of the Jaguar footwall volcanic rocks analyzed in this study match well with those
441 of Belford et al. (2015). The hanging-wall and footwall andesites from the Bentley deposit
442 show surprisingly similar geochemistry to those of the Jaguar footwall volcanic rocks. Given
443 the close spatial and temporal relationship between two areas, together with similar
444 geochemical features, the hanging-wall and footwall units of the Bentley and the footwall units
445 of the Jaguar are likely to be comagmatic and to have experienced similar magma
446 differentiation process. Rayleigh fractional crystallization models were conducted with

447 published mineral-melt partition coefficients for basalt and andesite melts (ESM Table 3) and
448 assumed crystallizing mineral assemblages. The results show that the trace element
449 geochemical variations from basalt, andesite to rhyolite, including PGE, are best explained by
450 fractional crystallization models with two stages (Fig. 5 and 6): Stage 1 (FC1) can be modeled
451 by Rayleigh fractionation of plagioclase + clinopyroxene + Cr-spinel (50:49:1), and Stage 2
452 (FC2) by fractional crystallization of plagioclase + clinopyroxene + magnetite (50:35:15) with
453 0.1 wt.% of sulfide liquid fraction. These mineral assemblages are consistent with the
454 occurrence of phenocrysts in the Jaguar and Bentley volcanic rocks (Belford, 2010) and
455 experimental studies of basaltic systems (e.g., Toplis and Carroll, 1995). Formation of andesite,
456 with arc-like signatures, can also be produced by mixing between plume-related basalts and
457 crustal melts as suggested for Archean volcanic rocks from the Kurnalpi terrane by Barnes and
458 Kranendonk (2014). The Ni and Cr contents in the less-evolved andesite range up to 109 and
459 143 ppm, respectively, which are higher than those of modern island arc andesites (Barnes and
460 Kranendonk, 2014). This implies that the parental magma of the Jaguar and Bentley volcanic
461 rocks may have been produced by processes that differ from those that produce the modern arc
462 systems. However, the mixing model cannot be applied for the Jaguar and Bentley systems
463 because it does not account for the geochemical trends displayed by Ti, V, and PGE that reach
464 their maximum and abruptly decrease in andesite (Fig. 5 and 6).

465

466 Sulfide saturation

467 Recent PGE geochemistry studies of intermediate and felsic igneous rocks (Park et al., 2013,
468 2015) have shown that the PGE can be used as a sensitive sulfide saturation indicator in
469 evolving magmatic systems. Palladium, in particular, behaves incompatibly prior to sulfide
470 saturation, but its concentrations decrease rapidly once the magma becomes sulfide saturated,

471 and immiscible sulfide melts begin to segregate.

472 Pd, Pt, Rh, and Ir contents in the Jaguar and Bentley basalt and andesite increase slightly
473 with increasing Yb in the early stage magma differentiation, but their concentrations are
474 significantly depleted in samples with > 4 ppm Yb (Fig. 6). This suggests sulfide saturation
475 occurred at ~ 4 ppm Yb in the andesite magma. The fraction of sulfide melts in crystallizing
476 mineral assemblage is considered to be ~ 0.1 wt.% (Model FC2 in Fig. 6), assuming sulfide
477 saturation at ~ 4 ppm Yb. The sulfide fraction is consistent with those of sulfide melts
478 determined for other sulfide-saturated submarine volcanic systems (Jamais et al., 2008; Park et
479 al., 2013; 2015). The cause of the sulfide saturation can be partly ascribed to magnetite
480 crystallization. The Ti and V concentrations in the andesites increase with increasing Yb,
481 reaching their maximum at ~ 4 ppm Yb, and decrease in the sample with > 4 ppm Yb (Fig. 5e
482 and f). These trends indicate the onset of magnetite crystallization at 4 ppm Yb. Magnetite
483 crystallization has been suggested to be a trigger for sulfides saturation in evolving magmatic
484 systems (e.g., Jenner et al., 2010) by reducing Fe₂O₃ in the silicate melt and thereby lowering
485 its oxygen fugacity.

486 It should be noted that Ru behaves compatibly before sulfide saturation at 4 ppm Yb, which
487 is distinguished from the behavior of other Ir-group PGE (Ir and Ru) and Rh. This can be
488 attributed to the fractionation of Cr-spinel that has a higher affinity to Ru than Ir and Rh (Park
489 et al., 2017). Fractional crystallization model FC1 with 1 wt.% Cr-spinel fraction and $D_{\text{Ru}}^{\text{Cr-}}$
490 spinel-melt of 200 and $D_{\text{Rh,Ir}}^{\text{Cr-spinel-melt}}$ of 50 accounts for the variations in IPGE and Rh of sulfide-
491 undersaturated basalt and andesite (< 4 ppm Yb; Fig. 6).

492 The extremely low PGE content of rhyolites indicates that they were formed from a magma
493 that had experienced prolonged sulfide segregation. A spike in Pt-Ir-Rh in the least evolved
494 rhyolite sample, which is not accompanied by an increase in Pd, is considered to be a nugget

495 effect, rather than a magmatic signature. It cannot be a sulfide nugget because the presence of
496 a sulfide nugget would increase all of the PGE, particularly Pd. The sample may have included
497 a tiny Pt-rich alloy crystal as an inclusion in an early-formed mineral (e.g., Cocker et al., 2015)
498 although there is no sign of Pt alloy formation during the evolution of the Jaguar and Bentley
499 magma system.

500 The PGE concentrations in the limited number of analyzed dolerite samples ($n = 5$) decrease
501 as Yb contents increase (Fig. 6), which suggests early sulfide saturation in a differentiating
502 magma. They show sub-parallel PGE patterns despite more than an order of magnitude
503 variation in absolute abundances (Fig. 7b). This implies that their PGE concentrations are
504 controlled by the removal of immiscible sulfide melt because the partition coefficients of PGE
505 to the sulfide melts are similar to each other. The cause of sulfide saturation in the dolerites is
506 not clear, but magnetite crystallization can be excluded because Ti and V concentrations
507 increase continuously during magma differentiation (Fig. 5e and g).

508

509 Sources for Cu and Au

510 As noted in the introduction, two sources have been proposed for the ore metals in the VMS
511 deposit: the footwall strata to the VMS deposit and a direct contribution from magmatic-
512 hydrothermal fluids (Franklin et al. 2005). A recent S isotope study (Chen et al., 2015) of the
513 sulfides from the Teutonic Bore, Jaguar and Bentley deposits showed that the S isotopic
514 composition of ore sulfides are consistent with the S being mainly of mantle origin ($\delta^{34}\text{S} = -$
515 0.83 to $+1.89\text{‰}$; $\Delta^{33}\text{S} = -0.46$ to -0.05‰) and distinct from sedimentary sulfides ($\delta^{34}\text{S} = +0.88$
516 to $+14.86\text{‰}$; $\Delta^{33}\text{S} = +0.19$ to $+6.20 \text{‰}$) both locally and regionally. Chen et al. (2015) suggested
517 the mantle S is likely to be derived from a magmatic-hydrothermal fluid, rather than from

518 magmatic sulfides in the footwall volcanic rocks by leaching based on several lines of evidence.
519 The sulfur contents of Archean marine sediments and Neoproterozoic shales are < ~10 wt.%
520 (Leshner et al., 1981) and ~2.5 wt.% (Stüeken et al., 2012), respectively, whereas those of
521 unmineralized volcanic rocks from Teutonic Bore and Kambalda are significantly lower
522 <<~0.1 wt.% (Leshner et al., 1981; Chen et al., 2015), showing substantial sulfur enrichment in
523 metasedimentary rocks. Also, massive sulfide ore bodies of the Teutonic Bore, Jaguar and
524 Bentley are either hosted by and/or underlain by sedimentary rock units containing sulfur-rich
525 shale layers or lenses with thicknesses of up to 70 m (Hallberg and Thompson, 1985; Belford,
526 2010; Parker et al., 2017). Therefore, if the sulfur in the VMS ores dominantly came from the
527 footwall strata by leaching, $\Delta^{33}\text{S}$ values of the ores should be positive or at least trend toward
528 positive values, which is not shown by the Chen et al. (2015) study.

529 Recent studies of the PGE geochemistry of submarine basalt to rhyolite suites showed that
530 the PGE, particularly Pd, can represent chalcophile element fertilities in evolving magmatic
531 systems (Park et al., 2013; Park et al., 2015). The PGE geochemistry of the Jaguar and Bentley
532 volcanic rocks showed that the andesites, before sulfide saturation, are the most fertile (i.e.,
533 chalcophile element-rich) among the footwall volcanic rocks at Jaguar and Bentley.
534 Furthermore, the footwall andesites are typically amygdaloidal (Belford, 2010), suggesting
535 they are volatile-saturated. Therefore, it is likely that the Jaguar and Bentley ore is formed from
536 a Cu-bearing magmatic-hydrothermal fluid that is exsolved from an underlying magma
537 chamber that fed the andesite magma. The rhyolite is extremely depleted in PGE and, therefore,
538 an unlikely source for Cu. Some dolerites are fertile enough to produce Cu mineralization.
539 However, they postdate the mineralization at both Jaguar and Bentley (Belford et al., 2015).

540 It might be argued that the mantle-like sulfur isotope composition of the Jaguar and Bentley
541 ore sulfide were derived from the footwall volcanic rocks. The total Cu tonnages are 49,600

542 tons for Jaguar and 61,000 tons for Bentley (Hollis et al., 2017). A simple mass balance
543 calculation has been carried out to find the volume of the footwall andesite, the most Cu-rich
544 lithology in this system (average Cu = ~50 ppm), which must be leached by a hydrothermal
545 fluid to produce the observed Cu tonnages. If it is assumed that the leaching and precipitation
546 efficiencies are 40 % and 15 %, respectively, as suggested by Patten et al. (2016; 2017) for
547 SMS systems, the results show that ~ 3.5 km³ and ~4.3 km³ of andesite are required to form
548 the Jaguar and Bentley Cu ores. This shows that most of the footwall units of the Jaguar and
549 Bentley deposits would need to be composed of andesite, to produce a ~5 km³ hydrothermal
550 cell similar in size to those that gave rise to the modern SMS deposits of the Eastern Pacific
551 Rise (Tolstoy et al., 2008). This is not possible for the Bentley. Although the andesites are one
552 of the major footwall units at the Bentley (Parker et al., 2017), the footwall lithology is
553 dominantly composed of Cu-depleted rhyolite (~17 ppm Cu; Table 2) with minor basalt in the
554 Bentley (Parker et al., 2017). Therefore, it is likely that additional Cu from a magmatic fluid
555 exsolved from an underlying magma chamber is necessary to form the Bentley Cu ores unless
556 abnormally efficient leaching and precipitation processes occurred in the source areas.

557

558 Chalcophile element fertility and implications for Au-rich VMS mineralization

559 Early studies of Archean VMS deposits showed that they are typically associated with felsic
560 volcanic rocks with specific geochemical characteristics (Leshner et al., 1986; Lentz, 1998).
561 Hart et al. (2004) reviewed all of the fertility models suggested previously and classified the
562 felsic volcanic rocks as FI, FII, FIII, and FIV types based on La/Yb and Yb concentrations.
563 They suggested that FIII and FIV types of rhyolites often host large VMS deposits (i.e., fertile),
564 FII type can hosts VMS deposits, but is commonly barren, and FI type rhyolites are usually
565 barren. Hart et al. (2004) suggested that the compositional variations between these types result

566 from the combined effects of differences in mineralogy, source composition, and the pressure
567 and temperature at which partial melting takes place. High-temperature melts, produced and
568 emplaced at shallow depths during extension (FIII affinity), are often associated with Archean
569 VMS deposits (Leshner et al., 1986; Hart et al., 2004). In a review of felsic and intermediate
570 volcanic rocks of the Yilgarn Craton, Hollis et al. (2015) found that the VMS-bearing volcanic
571 suites commonly display FII to dominantly FIII characteristics with high HFSE (Y, Zr, Sc)
572 concentrations, slight LREE enrichment ($La_N/Yb_N < 3$), and flat HREE patterns ($Dy_N/Yb_N \sim 1$).
573 Geochemistry of rhyolite and andesite from the Teutonic Bore, Jaguar and Bentley is in line
574 with other VMS-bearing volcanic rocks of the Yilgarn Craton, displaying FII and FIII affinities
575 (Fig. 9) and flattish REE profiles (Fig. 4). Although the magma fertility models based on
576 lithophile trace element geochemistry provide useful information on VMS ore genesis and
577 mineral exploration, they cannot account for variations in Cu and Au grades between different
578 VMS systems.

579 Recent studies on PGE geochemistry of porphyry deposits (Cocker et al., 2015; Hao et al.,
580 2017; 2019 Lowczak et al., 2018; Park et al., 2019) suggested that the PGE contents of volcanic
581 rocks can be used as a Cu and Au prospectivity indicator. They showed that the sub-volcanic
582 or volcanic suites associated with porphyry Cu and Cu-Au deposits are significantly enriched
583 in PGE at a given level of fractional crystallization compared to the barren suites. The PGE
584 contents of the felsic rocks also vary depending on the ore types (Cu-only vs. Cu-Au). The
585 rocks associated with Cu-Au porphyry deposits have higher PGE concentrations at a given
586 MgO content than those associated with Cu-only porphyry deposits. The PGE-depleted barren
587 rocks form from a magma that has undergone prolonged sulfide segregation and lost most of
588 its endowment of Cu, Au, and PGE in the solidifying magma chamber. In contrast, the PGE-
589 enriched fertile rocks crystallize from a magma that has either not experienced sulfide

590 saturation or precipitated a minimal amount of sulfide melt prior to volatile exsolution (Park et
591 al., 2019).

592 Figure 10 shows the volcanic rocks from Jaguar and Bentley plotted on the porphyry Cu±Au
593 fertility diagram proposed by Park et al. (2019) to show the difference between ore-bearing and
594 barren volcanic and intrusive magmatic suites. Pd is normalized by MgO to take into account
595 variations in fractionation, and Pd/Pt is a measure of the amount of fractional crystallization
596 before sulfide saturation (Park et al. 2019). We have also plotted PGE data for volcanic rocks
597 from two modern seafloor Cu-Au SMS deposits at arc-related settings: Pual Ridge
598 (PACMANUS hydrothermal field), Eastern Manus Basin, and the Niuatahi-Motutahi, Tonga
599 rear arc, for comparison (Binns and Scott, 1993; Kim et al., 2011; Berkenbosch et al., 2015;
600 Park et al. 2013b; 2015). The high Au contents in their ores were attributed to a large degree of
601 magmatic-hydrothermal fluid contributions (Moss et al., 2001; Kim et al., 2011; Berkenbosch
602 et al., 2015; Fuchs et al., 2019).

603 The pre-sulfide saturation andesites (< 4 ppm Yb) from the Jaguar and Bentley deposits
604 plot in the Cu-only porphyry field, but the remainder of the samples plot in the barren porphyry
605 field. The volcanic rocks from the Pual Ridge plot mostly in the Cu only field, whereas those
606 from Niuatahi-Motutahi plot mostly in the Cu-Au field but extend into the Cu only field. The
607 systematic depletion of chalcophile element fertility indicators, Pd/MgO and Pd/Pt, in the
608 Jaguar and Bentley rocks compared with the two modern Cu-Au SMS deposits suggests that
609 the Jaguar and Bentley magmas may have undergone sulfide saturation at an earlier stage of
610 differentiation than Pual Ridge and Niuatahi-Motutahi magmas, or that they have originated
611 from chalcophile element depleted sources. We suggest that sulfide saturation in the Jaguar and
612 Bentley magmas occurred before ore formation and that enough sulfide precipitated to deplete
613 the magma in Au but not Cu, because of the lower partition coefficient into immiscible sulfide

614 melts of the latter (Mungall and Brennan, 2014; Li and Audetat, 2015). As a consequence, the
615 Jaguar and Bentley deposits are Cu-rich but contain less Au than Pual Ridge and Niuatahi-
616 Motutahi. Bentley, for example, contains 0.7 g/t Au in the VMS ores (Hollis et al., 2017)
617 whereas Au grades are 10 g/t in Pual Ridge (PACMANUS; Fuchs et al., 2019) and 14 g/t in
618 Niuatahi-Motutahi (also known as Volcano O and MTJ; Fuchs et al., 2019). The Au grade of
619 0.7 g/t for the Bentley ore is at the lower end of the range of Au grades (0.24 to 6.2 g/t Au) for
620 the Archean VMS deposits in the Yilgarn Craton (Hollis et al., 2017).

621 Although the fertility diagram (Fig. 10), based on studies of porphyry deposits, generally
622 match well with the SMS and VMS systems, care needs to be taken for its application because,
623 unlike the porphyry system where metals are dominantly sourced from a magma, some portion
624 of the ore metals are thought to be leached from country rocks below the VMS deposits.
625 Furthermore, this method cannot be applied for Pb and Zn deposits because Pb and Zn are only
626 moderately chalcophile and not significantly influenced by sulfide saturation during magma
627 differentiation.

628

629 **Conclusions**

630 The trace element and PGE geochemistry of basalt, andesite, and rhyolites from the footwall
631 of the Jaguar and footwall and hanging-wall of the Bentley are similar to each other. Their
632 compositions are comparable to those of Phanerozoic calc-alkaline island arc volcanic rocks,
633 showing fractionated primitive mantle normalized trace element patterns with marked negative
634 Nb and Ti anomalies. Their geochemical similarity, together with the close temporal and spatial
635 relationship, suggests their comagmatic origin. The geochemical variations in trace elements
636 from basalt through andesite to rhyolite can be accounted for by fractional crystallization.

637 Sulfide saturation occurred late in the evolution of the andesite magma with magnetite
638 crystallization as a likely trigger. The rhyolites are extremely depleted in all PGEs. The
639 dolerites are geochemically distinct from the other rock types and show typical sulfide saturated
640 magma differentiation from the early stage of magma evolution. The least evolved dolerites
641 are fertile, but they cannot be related to the ore formation because they post-date the
642 mineralization.

643 The PGE data of the Jaguar and Bentley volcanic rocks suggest that Cu in the ore sulfide
644 was principally formed from a magmatic fluid exsolved from the andesite magma shortly after
645 sulfide saturation. The chalcophile element fertility of the Jaguar and Bentley magma is
646 significantly lower than that of volcanic rocks associated with Cu-Au SMS deposits, which is
647 consistent with Cu-Zn mineralization in the Jaguar and Bentley VMS deposits. These results
648 suggest chalcophile element fertility may play an important role in the formation of the ancient
649 VMS and modern SMS deposits, particularly with respect to Au grade when the magmatic-
650 hydrothermal component is the dominant source for metals in VMS systems.

651

652 Acknowledgment

653 The authors would like to thank two reviewers, Stephen Barnes and Steven Hollis, and the
654 associated editor, Marco Fiorentini, for their critical and constructive comments that improved
655 the manuscript substantially. Hongda Hao and Helen Coker are thanked for their assistance
656 with the whole-rock major and PGE analyses. We also thank Mimi Chen for the discussion on
657 samples and local geology. This research was funded by the ARC Linkage Project
658 LP110200747, and we thank its sponsors, particularly the Independence Group, for access to
659 the Jaguar and Bentley VMS deposits and to their geochemical and petrological data. We also

660 acknowledge that part of this study was supported by the National Research Foundation (NRF)
661 of Korea grant funded by the Korea government (No. 2019R1A2C1009809) for a project
662 entitled 'Understanding the deepsea biosphere on seafloor hydrothermal vents in the Indian
663 Ridge (No. 20170411)' funded by the Ministry of Oceans and Fisheries, Korea.

664

665 Figure captions

666 Figure 1. a) Large scale tectonic segments of the Yilgarn craton with locations of Teutonic Bore,
667 Jaguar, and Bentley VMS deposits (modified from Belford, 2010). b) Regional geology map
668 of the Teutonic Bore volcanic complex, Western Australia produced by Max Frater and
669 geologists of Independence Group NL. Solid lines represent faults.

670 Figure 2. Simplified drill hole logs of Jaguar (13JUDD002, 12 JADD002) and Bentley
671 (09BTDD029, 09BTDD025) VMS deposits based on the core logs of Independence Group NL
672 geologists.

673 Figure 3. Primitive mantle normalized incompatible trace element diagrams for the Jaguar and
674 Bentley rhyolite/Dacite (a), andesite (b), basalt (c), and dolerite (d). Phanerozoic island arc
675 fields are from Barnes and Van Kranendonk (2014). Primitive mantle values are from
676 McDonough and Sun (1995).

677 Figure 4. Chondrite-normalized REE variation diagrams for a) rhyolite, b) andesite, c) basalt,
678 d) dolerite from Jaguar and Bentley. Dark and light gray fields represent the patterns of volcanic
679 rocks from Jaguar reported by Belford (2010).

680 Figure 5. Binary plots of a) La, b) Zr, c) Cr, d) Ni, e) Ti, and f) V against Yb concentrations for
681 the Jaguar and Bentley volcanic rocks. Yb concentration is a measure of the degree of
682 fractionation crystallization. Solid (FC1) and dashed lines (FC2) are fractional crystallization
683 models. FC1 represents fractional crystallization trends for plagioclase + clinopyroxene + Cr-
684 spinel (50:49:1) with the initial concentrations of a basalt (sample 44907). FC2 represents
685 trends for plagioclase + clinopyroxene + magnetite (50:35:15) with an immiscible sulfide liquid
686 fraction of 0.1 wt.%. The initial concentrations for FC2 are set as melt composition after 43%
687 fractional crystallization of FC1. Thin crosses on the model curves show 10% fractional
688 crystallization intervals. Partition coefficients used are given in ESM Table 3.

689 Figure 6. Binary plots of a) Pd, b) Rh, c) Pt, d) Ru, e) Ir, and f) Cu against Yb, as a fractionation
690 index. Solid (FC1) and dashed lines (FC2) are fractional crystallization models. FC1 displays
691 fractional crystallization trends for plagioclase + clinopyroxene + Cr-spinel (50:49:1). The
692 compositions of a basalt (sample 44907) are set as the initial concentrations for all elements
693 except Pd and Rh for which the compositions of andesite sample 44619 are used. FC2 shows
694 trends for plagioclase + clinopyroxene + magnetite (50:35:15) with an immiscible sulfide liquid
695 fraction of 0.1 wt.%. The melt compositions after 43% fractional crystallization of FC1 are
696 used as initial concentrations for FC2. Thin crosses on the curves show 10% fractional
697 crystallization intervals. Partition coefficients used are given in ESM Table 3. Dotted lines
698 represent the method detection limit for PGEs.

699 Figure 7. Primitive mantle normalized PGE and Re patterns. The arc andesite field is from Park
700 et al. (2013) (Sample MD53a, MD53b, MD7 with MgO ranging from 1.7 to 3.0 wt.%). Dotted
701 lines represent the method detection limit for PGEs.

702 Figure 8. An alteration box plot for Jaguar and Bentley volcanic rocks. Fields of least altered
703 felsic, intermediate, and mafic rocks are from the Rosebery, Que River, and Hellyer areas of
704 the Mount Read volcanics (Large et al., 2001 and references therein)

705 Figure 9. A chondrite-normalized plot of Yb vs. La/Yb. The fields of each rhyolite type are
706 from Hart et al. (2004). The data of volcanic rocks associated with Golden Grove, Hollandaire,
707 Quinns Archean VMS deposits in the Yuanmi terrane are from Hollis et al. (2015) and
708 references therein.

709 Figure 10. Binary plots of Pd/MgO vs. Pd/Pt. The fields for barren porphyries, Cu porphyries,
710 Cu-Au porphyries are from Park et al. (2019).

711 **References**

- 712 Barley ME, Brown SJA, Krapez B, Kositcin N (2008) Physical volcanology and geochemistry of a Late
713 Archaean volcanic arc: Kurnalpi and Gindalbie Terranes, Eastern Goldfields Superterrane,
714 Western Australia. *Precambrian Res* 161:53-76
- 715 Barnes SJ, Van Kranendonk MJ (2014) Archean andesites in the east Yilgarn craton, Australia: Products
716 of plume-crust interaction? *Lithosphere* 6:80-92
- 717 Belford S (2010) Genetic and Chemical Characterisation of the Host Succession to the Archean Jaguar
718 VHMS Deposit. University of Tasmania
- 719 Belford SM, Davidson GJ, McPhie J, Large RR (2015) Architecture of the Neoproterozoic Jaguar VHMS
720 deposit, Western Australia: Implications for prospectivity and the presence of depositional
721 breaks. *Precambrian Res* 260:136-160
- 722 Berkenbosch HA, de Ronde CEJ, Gemmill JB, McNeill AW, Goemann K (2012) Mineralogy and
723 Formation of Black Smoker Chimneys from Brothers Submarine Volcano, Kermadec Arc. *Econ*
724 *Geol* 107:1613-1633
- 725 Berkenbosch HA, de Ronde CEJ, Paul BT, Gemmill JB (2015) Characteristics of Cu isotopes from
726 chalcopyrite-rich black smoker chimneys at Brothers volcano, Kermadec arc, and Niutahi
727 volcano, Lau basin. *Miner Deposita* 50:811-824
- 728 Binns RA, Scott SD (1993) Actively forming polymetallic sulfide deposits associated with felsic
729 volcanic rocks in the eastern Manus back-arc basin, Papua New Guinea. *Econ Geol* 88:2226-
730 2236
- 731 Brown SJA, Barley ME, Krapež B, Cas RAF (2002) The Late Archaean Melita Complex, Eastern
732 Goldfields, Western Australia: shallow submarine bimodal volcanism in a rifted arc
733 environment. *J Volcanol Geoth Res* 115:303-327
- 734 Butterfield DA, Nakamura K, Takano B, Lilley MD, Lupton JE, Resing JA, Roe KK (2011) High SO₂
735 flux, sulfur accumulation, and gas fractionation at an erupting submarine volcano. *Geology*
736 39:803-806
- 737 Campbell IH, Franklin JM, Gorton MP, Hart TR, Scott SD (1981) The Role of Subvolcanic Sills in the
738 Generation of Massive Sulfide Deposits. *Econ Geol* 76:2248-2253
- 739 Cassidy KF, Champion DC, Fletcher IR, Dunphy JM, Black LP, Clauue-Long JC (2002)
740 Geochronological constraints on the Leonora-Laverton transect area, northeastern Yilgarn
741 Craton, Geology, geochronology and geophysics of the northeastern Yilgarn Craton, with an
742 emphasis on the Leonora-Laverton transect area; proceedings of papers presented at an industry
743 workshop, Australian Geological Survey Organisation, 37-58
- 744 Chen MM et al. (2015) Multiple Sulfur Isotope Analyses Support a Magmatic Model for the
745 Volcanogenic Massive Sulfide Deposits of the Teutonic Bore Volcanic Complex, Yilgarn
746 Craton, Western Australia. *Econ Geol* 110:1411-1423
- 747 Cocker HA, Valente DL, Park JW, Campbell IH (2015) Using Platinum Group Elements to Identify
748 Sulfide Saturation in a Porphyry Cu System: the El Abra Porphyry Cu Deposit, Northern Chile.
749 *J Petrol* 56:2491-2514
- 750 Crocket JH (2000) PGE in fresh basalt, hydrothermal alteration products, and volcanic incrustations of
751 Kilauea volcano, Hawaii. *Geochim Cosmochim Acta* 64:1791-1807
- 752 de Ronde CEJ, Baker ET, Massoth GJ, Lupton JE, Wright IC, Feely RA, Greene RR (2001) Intra-
753 oceanic subduction-related hydrothermal venting, Kermadec volcanic arc, New Zealand. *Earth*
754 *Planet Sci Lett* 193:359-369
- 755 de Ronde CEJ et al. (2005) Evolution of a Submarine Magmatic-Hydrothermal System: Brothers
756 Volcano, Southern Kermadec Arc, New Zealand. *Econ Geol* 100:1097-1133
- 757 de Ronde CEJ, Hein JR, Butterfield DA (2014) Metallogenesis and Mineralization of Intraoceanic Arcs
758 II: The Aeolian, Izu-Bonin, Mariana, and Kermadec Arcs, and the Manus Backarc Basin-
759 Introduction. *Econ Geol* 109:2073-2077
- 760 de Ronde CEJ et al. (2011) Submarine hydrothermal activity and gold-rich mineralization at Brothers
761 Volcano, Kermadec Arc, New Zealand. *Miner Deposita* 46:541-584
- 762 Franklin JM et al. (2005) Volcanogenic Massive Sulfide Deposits. In: One Hundredth Anniversary

763 Volume. Society of Economic Geologists.

764 Fuchs S, Hannington MD, Petersen S (2019) Divining gold in seafloor polymetallic massive sulfide
765 systems. *Miner Deposita* 54:789-820

766 Gruen G, Weis P, Driesner T, Heinrich CA, de Ronde CEJ (2014) Hydrodynamic modeling of
767 magmatic-hydrothermal activity at submarine arc volcanoes, with implications for ore
768 formation. *Earth Planet Sci Lett* 404:307-318

769 Hallberg JA (1984) A Geochemical Aid to Igneous Rock Type Identification in Deeply Weathered
770 Terrain. *J Geochem Explor* 20:1-8

771 Hallberg JA, Thompson JFH (1985) Geologic Setting of the Teutonic Bore Massive Sulfide Deposit,
772 Archean Yilgarn Block, Western Australia. *Econ Geol* 80:1953-1964

773 Hao HD, Campbell IH, Park JW, Cooke DR (2017) Platinum-group element geochemistry used to
774 determine Cu and Au fertility in the Northparkes igneous suites, New South Wales, Australia.
775 *Geochim Cosmochim Acta* 216:372-392

776 Hao HD, Campbell IH, Richards JP, Nakamura E, Sakaguchi C (2019) Platinum-Group Element
777 Geochemistry of the Escondida Igneous Suites, Northern Chile: Implications for Ore Formation.
778 *J Petrol* 60:487-514

779 Hart TR, Gibson HL, Leshner CM (2004) Trace element geochemistry and petrogenesis of felsic volcanic
780 rocks associated with volcanogenic massive Cu-Zn-Pb sulfide deposits. *Econ Geol Bull Soc*
781 99:1003-1013

782 Hayman P, Cas, R., Squire, R. J., Das, R., Wingate, S., Wyche, S., Amelin, Y., Campbell, I., Chen, M.,
783 Allen, C., Uren, A., Xue, Y. (2014) Age constraints for the Teutonic Bore volcanic complex
784 from thermal ionisation mass spectrometry, Geochronology report. presented to Sixth
785 Sponsors Meeting, Kalgoorlie, November, 12p

786 Hollis SP, Yeats, C.J., Wyche, S., Barnes, S.J. and Ivanic, T.J. (2017) VMS mineralization in the
787 Yilgarn Craton, Western Australia: a review of known deposits and prospectivity analysis of
788 felsic volcanic rocks. Geological Survey of Western Australia, Report 165, 68p.

789 Hollis SP, Yeats, C. J., Wyche, S., Barnes, S. J., Ivanic, T. J., Belford, S. M., Davidson, G. J., Roache,
790 A. J., Wingate, M. T. D. (2015) A review of volcanic-hosted massive sulfide (VHMS)
791 mineralization in the Archean Yilgarn Craton, Western Australia: Tectonic, stratigraphic and
792 geochemical associations *Precambrian Res* 260:113-135

793 Huston DL (1997) Stable Isotopes and Their Significance for Understanding the Genesis of Volcanic-
794 Hosted Massive Sulfide Deposits: A Review. In: *Volcanic Associated Massive Sulfide*
795 *Deposits: Processes and Examples in Modern and Ancient Settings*, vol 8. Society of Economic
796 Geologists.

797 Huston DL, Relvas JMRS, Gemmell JB, Drieberg S (2011) The role of granites in volcanic-hosted
798 massive sulphide ore-forming systems: an assessment of magmatic-hydrothermal contributions.
799 *Miner Deposita* 46:473-507

800 Jamais M, Lassiter JC, Brugmann G (2008) PGE and Os-isotopic variations in lavas from Kohala
801 Volcano, Hawaii: Constraints on PGE behavior and melt/crust interaction. *Chem Geol* 250:16-
802 28

803 Jenner FE, O'Neill HSC, Arculus RJ, Mavrogenes JA (2010) The Magnetite Crisis in the Evolution of
804 Arc-related Magmas and the Initial Concentration of Au, Ag and Cu. *J Petrol* 51:2445-2464

805 Jochum KP, Nohl U (2008) Reference materials in geochemistry and environmental research and the
806 GeoReM database. *Chem Geol* 253:50-53

807 Kim J, Lee K-Y, Kim J-H (2011) Metal-bearing molten sulfur collected from a submarine volcano:
808 Implications for vapor transport of metals in seafloor hydrothermal systems. *Geology* 39:351-
809 354

810 Kositcin N, Brown SJA, Barley ME, Krapez B, Cassidy KF, Champion DC (2008) SHRIMP U-Pb
811 zircon age constraints on the Late Archean tectonostratigraphic architecture of the Eastern
812 Goldfields Superterrane, Yilgarn Craton, Western Australia. *Precambrian Res* 161:5-33

813 Large RR, Gemmell JB, Paulick H, Huston DL (2001) The Alteration Box Plot: A Simple Approach to
814 Understanding the Relationship between Alteration Mineralogy and Lithochemistry
815 Associated with Volcanic-Hosted Massive Sulfide Deposits *Econ Geol* 96:957-971

816 Lentz DR (1998) Petrogenetic evolution of felsic volcanic sequences associated with Phanerozoic

817 volcanic-hosted massive sulphide systems: the role of extensional geodynamics. *Ore Geology*
818 *Reviews* 12:289-327

819 Leshner CM, Goodwin AM, Campbell IH, Gorton MP (1986) Trace-element geochemistry of ore-
820 associated and barren, felsic metavolcanic rocks in the Superior Province, Canada. *Can J Earth*
821 *Sci* 23:222-237

822 Li Y, Audétat A (2015) Effects of temperature, silicate melt composition, and oxygen fugacity on the
823 partitioning of V, Mn, Co, Ni, Cu, Zn, As, Mo, Ag, Sn, Sb, W, Au, Pb, and Bi between sulfide
824 phases and silicate melt. *Geochim Cosmochim Acta* 162:25-45

825 Lowczak JN, Campbell IH, Cocker H, Park JW, Cooke DR (2018) Platinum-group element
826 geochemistry of the Forest Reef Volcanics, southeastern Australia: Implications for porphyry
827 Au-Cu mineralisation. *Geochim Cosmochim Acta* 220:385-406

828 Lupton J et al. (2006) Submarine venting of liquid carbon dioxide on a Mariana Arc volcano. *Geochem*
829 *Geophys Geosy*. <https://doi.org/10.1029/2005GC001152>

830 Lupton J et al. (2008) Venting of a separate CO₂-rich gas phase from submarine arc volcanoes:
831 Examples from the Mariana and Tonga-Kermadec arcs. *J Geophys Res-Sol Ea*.
832 <https://doi.org/10.1029/2007JB005467>

833 MacLean WH, Barrett TJ (1993) Lithochemical Techniques Using Immobile Elements. *J Geochem*
834 *Explor* 48:109-133

835 Massoth GJ, De Ronde CEJ, Lupton JE, Feely RA, Baker ET, Lebon GT, Maenner SM (2003)
836 Chemically rich and diverse submarine hydrothermal plumes of the southern Kermadec
837 volcanic arc (New Zealand). *Geological Society, London, Special Publications* 219:119-139

838 McDonough WF, Sun SS (1995) The Composition of the Earth. *Chem Geol* 120:223-253

839 Meisel T, Moser J (2004) Platinum-group element and rhenium concentrations in low abundance
840 reference materials. *Geostand Geoanal Res* 28:233-250

841 Moss R, Scott SD, Binns RA (2001) Gold Content of Eastern Manus Basin Volcanic Rocks:
842 Implications for Enrichment in Associated Hydrothermal Precipitates. *Econ Geol* 96:91-107

843 Mungall JE, Brenan JM (2014) Partitioning of platinum-group elements and Au between sulfide liquid
844 and basalt and the origins of mantle-crust fractionation of the chalcophile elements. *Geochim*
845 *Cosmochim Acta* 125:265-289

846 Nelson, D. R., 1995, Compilation of SHRIMP U-Pb zircon geochronology data, 1994, Record 1995/3,
847 Western Australia Geological Survey.

848 Nelson DR (1997a) Evolution of the Archaean granite-greenstone terranes of the eastern goldfields,
849 Western Australia: SHRIMP U-Pb zircon constraints. *Precambrian Res* 83:57-81

850 Nelson, DR (1997b) Compilation of SHRIMP U-Pb zircon geochronology data, 1996, Record 1997/2,
851 Western Australia Geological Survey.

852 Park J-W, Campbell IH, Arculus RJ (2013) Platinum-alloy and sulfur saturation in an arc-related basalt
853 to rhyolite suite: Evidence from the Pual Ridge lavas, the Eastern Manus Basin. *Geochim*
854 *Cosmochim Acta* 101:76-95

855 Park J-W, Hu ZC, Gao S, Campbell IH, Gong HJ (2012) Platinum group element abundances in the
856 upper continental crust revisited - New constraints from analyses of Chinese loess. *Geochim*
857 *Cosmochim Acta* 93:63-76

858 Park J-W, Campbell IH, Kim J (2016) Abundances of platinum group elements in native sulfur
859 condensates from the Niuatahi-Motutahi submarine volcano, Tonga rear arc: Implications for
860 PGE mineralization in porphyry deposits. *Geochim Cosmochim Acta* 174:236-246

861 Park J-W, Campbell IH, Kim J, Moon JW (2015) The Role of Late Sulfide Saturation in the Formation
862 of a Cu- and Au-rich Magma: Insights from the Platinum Group Element Geochemistry of
863 Niuatahi-Motutahi Lavas, Tonga Rear Arc. *J Petrol* 56:59-81

864 Park J-W, Campbell IH, Malaviarachchi SPK, Cocker H, Hao HD, Kay SM (2019) Chalcophile element
865 fertility and the formation of porphyry Cu±Au deposits. *Miner Deposita* 54:657-670

866 Park J-W, Kamenetsky V, Campbell I, Park G, Hanski E, Pushkarev E (2017) Empirical constraints on
867 partitioning of platinum group elements between Cr-spinel and primitive terrestrial magmas.
868 *Geochim Cosmochim Acta* 216:393-416

869 Parker P, Belford SM, Maier R, Lynn S, Stewart W (2017) Teutonic Bore - Jaguar - Bentley
870 volcanogenic massive sulfide field. In: Phillips GN (ed) *Australian Ore Deposits*, vol 32. The

- 871 Australian Institute of Mining and Metallurgy, Melbourne, pp 167-172
872 Patten CGC, Pitcairn IK, Teagle DAH (2017) Hydrothermal mobilisation of Au and other metals in
873 supra-subduction oceanic crust: Insights from the Troodos ophiolite. *Ore Geology Reviews*
874 86:487-508
875 Patten CGC, Pitcairn IK, Teagle DAH, Harris M (2016) Mobility of Au and related elements during
876 the hydrothermal alteration of the oceanic crust: implications for the sources of metals in
877 VMS deposits. *Miner Deposita* 51(2):179-200
878 Patten CGC, Pitcairn IK, Alt JC, Zack T, Lahaye Y, Teagle DAH, Markdahl K (2020) Metal fluxes
879 during magmatic degassing in the oceanic crust: sulfide mineralisation at ODP site 786B, Izu-
880 Bonin forearc *Miner Deposita* 55:469-489
881 Pearce JA, Cann JR (1973) Tectonic Setting of Basic Volcanic-Rocks Determined Using Trace-Element
882 Analyses. *Earth Planet Sci Lett* 19:290-300
883 Peucker-Ehrenbrink B, Bach W, Hart SR, Blusztajn JS, Abbruzzese T (2003) Rhenium-osmium isotope
884 systematics and platinum group element concentrations in oceanic crust from DSDP/ODP Sites
885 504 and 417/418. *Geochem Geophys Geosy* <https://doi.org/10.1029/2002GC000414>
886 Resing JA, Baker ET, Lupton JE, Walker SL, Butterfield DA, Massoth GJ, Nakamura K (2009)
887 Chemistry of hydrothermal plumes above submarine volcanoes of the Mariana Arc. *Geochem*
888 *Geophys Geosy*. <https://doi.org/10.1029/2008GC002141>
889 Resing JA et al. (2007) Venting of Acid-Sulfate Fluids in a High-Sulfidation Setting at NW Rota-1
890 Submarine Volcano on the Mariana Arc. *Econ Geol* 102:1047-1061
891 Swager CP (1997) Tectono-stratigraphy of late Archaean greenstone terranes in the southern eastern
892 goldfields, Western Australia. *Precambrian Res* 83:11-42
893 Swager CP, Witt WK, Griffin TJ, Ahmat AL, Hunter WM, McGoldrick PJ, Wyche S (1992) Late
894 Archaean granite–greenstones of the Kalgoorlie Terrane, Yilgarn Craton, Western Australia, in
895 Glover, J. E., and Ho, S. E., eds., *The Archaean: terrains, processes and metallogeny*, The
896 University of Western Australia, Geology Department and University Extension, Publication
897 no. 22, p. 107–122.
898 Tolstoy M, Waldhauser F, Bohnenstiehl DR, Weekly RT, Kim WY (2008) Seismic identification of
899 along-axis hydrothermal flow on the East Pacific Rise. *Nature* 451(7175):181-184
900 Toplis MJ, Carroll MR (1995) An Experimental Study of the Influence of Oxygen Fugacity on Fe-Ti
901 Oxide Stability, Phase Relations, and Mineral—Melt Equilibria in Ferro-Basaltic Systems. *J*
902 *Petrol* 36:1137-1170
903 Whitford DJ, Cameron MA (1987) Trace-Element Geochemistry of Ore-Associated and Barren, Felsic
904 Metavolcanic Rocks in the Superior-Province, Canada – Discussion. *Can J Earth Sci* 24:1498-
905 1500
906 Whitford DJ, Mcpherson WPA, Wallace DB (1989) Geochemistry of the Host Rocks of the
907 Volcanogenic Massive Sulfide Deposit at Que River, Tasmania. *Econ Geol* 84:1-21
908 Winchester JA, Floyd PA (1977) Geochemical Discrimination of Different Magma Series and Their
909 Differentiation Products Using Immobile Elements. *Chem Geol* 20:325-343
910 Yang KH, Scott SD (1996) Possible contribution of a metal-rich magmatic fluid to a sea-floor
911 hydrothermal system. *Nature* 383:420-423

912

Table 1. Whole-rock major element composition of the Jaguar and Bentley volcanic rocks by XRF (wt.%)

Samples	Core No.	Na ₂ O	MgO	Al ₂ O ₃	SiO ₂	FeO	MnO	K ₂ O	CaO	TiO ₂	P ₂ O ₅	Total	LOI	SO ₃
<i>Recalculated compositions on a volatile-free basis</i>														
<i>Rhyolite</i>														
JB Rhy-02	13TRDD014	0.86	1.20	10.5	81.7	2.0	0.04	1.63	1.89	0.17	0.02	100	4.06	0.03
JB 44681	13JUDD002	0.31	1.89	10.5	76.9	4.1	0.06	5.05	1.03	0.15	0.02	100	2.26	b.d.l.
JB 44913	09BTDD025	0.30	2.10	10.9	76.5	4.6	0.11	2.33	2.86	0.22	0.02	100	5.48	0.47
JB 44922	09BTDD025	0.18	2.88	10.9	78.0	5.5	0.05	2.23	0.04	0.17	0.02	100	4.13	0.22
JB dac-01	12TRDD016	1.48	4.33	15.2	60.7	8.3	0.10	3.22	5.27	1.14	0.24	100	4.79	b.d.l.
<i>Andesite</i>														
JB 44663	13JUDD002	4.96	6.39	16.7	57.2	8.1	0.12	0.34	5.30	0.79	0.15	100	6.28	0.02
JB 44665	13JUDD002	2.81	6.24	16.8	56.4	7.9	0.16	0.89	7.85	0.77	0.15	100	3.64	0.02
JB 44640	09BTDD029	3.22	1.31	14.2	68.1	5.7	0.19	1.64	4.62	0.77	0.25	100	4.97	0.01
JB 44904	09BTDD025	4.33	0.93	16.2	63.7	4.3	0.22	1.99	7.24	0.90	0.28	100	6.57	0.03
JB 44906	09BTDD025	0.52	2.61	12.8	71.9	6.8	0.09	2.17	1.84	0.93	0.35	100	3.55	0.37
JB 44613	09BTDD029	5.82	5.30	16.1	58.7	6.8	0.13	0.05	5.53	1.25	0.30	100	5.51	0.11
JB 44616	09BTDD029	3.82	5.59	15.8	58.6	7.4	0.13	0.98	6.27	1.18	0.29	100	6.48	0.13
JB and-01	12TRDD016	1.31	1.37	12.7	75.5	4.3	0.05	2.86	1.58	0.35	0.08	100	10.7	0.35
JB and-02	13TRDD009	1.45	2.82	15.0	64.2	7.3	0.09	2.78	5.28	0.96	0.21	100	8.58	0.14
JB and-03	13TRDD009	2.29	2.80	14.7	66.0	6.2	0.07	2.43	4.42	0.90	0.19	100	7.46	0.19
<i>Basalt</i>														
JB 44677	13JUDD002	0.05	1.73	13.6	63.2	10.2	0.43	3.33	5.47	1.67	0.28	100	6.11	0.39
JB 44696	12JADD002	4.65	2.67	15.2	57.7	9.3	0.26	1.43	6.65	1.91	0.29	100	5.25	0.13
JB 44907	09BTDD025	2.10	2.53	15.6	57.1	4.9	0.22	2.12	13.99	1.17	0.25	100	11.7	0.26
<i>Dolerite</i>														
JB 44672	13JUDD002	2.47	4.53	13.1	52.1	16.5	0.26	0.51	8.54	1.84	0.13	100	2.31	0.53
JB 44673	13JUDD002	1.76	7.90	14.8	50.9	11.2	0.21	0.07	12.14	0.87	0.08	100	2.27	0.13
JB 44605	09BTDD029	2.25	7.21	13.8	55.2	11.9	0.17	0.19	7.97	1.16	0.12	100	4.60	0.07
JB Dol-01	09TRDD032	0.35	5.15	18.5	52.3	11.3	0.28	4.25	6.60	1.06	0.10	100	7.22	2.37
JB Dol-02	13TRDD001	0.40	3.58	16.0	55.3	18.5	0.11	1.67	3.48	0.86	0.08	100	11.9	0.42

b.d.l., below detection limit

Table 2. Whole-rock trace element composition of the Jaguar and Bentley volcanic rocks by LA-ICP-MS (ppm)

Lithology	Rhyolite						Dacite			Andesite								
	FW	FW	FW	MP	FW	FW	MP	MP	HW	HW	HW	HW	HW	HW	FW	FW	FW	
	Teutonic Bore	Jaguar	Jaguar	Bentley	Bentley	Bentley	Jaguar	Jaguar	Bentley	Bentley	Bentley	Bentley	Bentley	Bentley	Bentley	Bentley	Bentley	
Deposit	JB Rhy-02	JB 44681	JB 44699	JB 44913	JB 44922	JB dac-01	JB 44663	JB 44665	JB 44640	JB 44904	JB 44906	JB 44613	JB 44619	JB 44616	JB And-01	JB And-02	JB And-03	
Sample No.																		
Sc	7.9	8.3	6.3	11.4	8.8	12.2	28.5	27.9	18.7	20.4	16.2	33.2	n.a.	32.6	27.0	23.8	21.4	
Ti	973	841	1063	1177	967	2385	4973	4580	4671	5409	5381	7257	6109	6617	7710	6531	6068	
V	4.8	4.1	3.0	4.6	4.4	12.7	160	152	20.8	23.5	51.4	201	n.a.	197	169	150	118	
Cr	4.9	4.8	7.0	5.7	4.3	9.0	142.9	143.1	7.8	6.2	5.2	91.6	n.a.	120.1	78.4	26.8	22.5	
Mn	330	436	247	742	399	382	994	1157	1405	1592	695	936	n.a.	981	752	692	524	
Co	8.1	12.8	0.4	10.6	15.3	1.5	38.8	36.9	13.9	11.6	16.1	35.8	n.a.	39.0	28.6	20.0	12.6	
Ni	5.6	4.0	6.9	7.7	5.9	4.2	109.8	104.0	7.5	6.4	9.2	56.4	n.a.	84.9	46.4	35.6	21.7	
Cu	14.6	5.2	24.8	12.0	34.1	14.5	55.3	52.9	15.1	75.7	55.2	42.9	n.a.	61.7	58.8	72.7	8.0	
Zn	29	53	19	153	144	83	66	72	85	164	65	89	n.a.	87	83	64	49	
Rb	44.5	52.3	63.3	38.6	50.7	66.3	13.7	24.4	34.3	38.8	64.6	0.9	n.a.	21.0	72.3	68.3	60.7	
Sr	87.7	44.5	20.9	31.5	9.2	79.7	170.4	233.5	98.4	168.1	73.3	199.2	n.a.	149.2	153.5	103.7	92.7	
Y	56.3	54.2	39.5	42.3	47.3	46.2	20.2	18.4	43.1	45.0	36.7	34.6	27.3	29.9	38.6	39.0	42.0	
Zr	348	275	349	339	316	395	138	129	278	322	215	191	154	173	261	251	255	
Nb	17.3	12.1	15.7	14.3	14.5	17.2	8.5	7.6	11.5	13.4	9.5	9.7	7.6	9.4	11.7	11.6	12.2	
Cs	2.39	1.39	0.86	1.16	1.30	3.86	0.49	0.44	1.43	1.59	1.87	0.70	n.a.	3.49	3.61	6.32	6.20	
Ba	289	1159	1496	218	280	346	165	210	183	301	519	88	n.a.	297	396	463	440	
La	36.0	34.0	38.1	30.1	30.6	34.0	17.6	15.6	24.2	30.2	21.0	16.3	15.0	17.4	21.3	21.6	24.3	
Ce	80.1	74.2	83.1	64.1	71.2	77.0	34.1	30.9	54.3	64.5	48.4	39.4	35.2	38.8	49.3	50.7	55.4	
Pr	9.98	8.98	10.02	7.75	8.88	9.56	4.09	3.68	7.10	8.24	6.38	5.38	4.52	5.02	6.36	6.53	6.95	
Nd	41.5	36.3	39.8	31.1	36.3	39.9	16.7	14.9	30.2	34.8	27.7	24.1	20.6	21.9	27.6	27.8	29.6	
Sm	9.09	8.05	8.39	6.65	7.70	8.62	3.59	3.24	7.04	8.00	6.57	5.67	4.81	5.09	6.44	6.42	6.67	
Eu	1.79	1.69	1.72	1.36	0.97	1.56	1.07	1.07	1.69	2.12	1.42	1.50	1.49	1.42	1.56	1.55	1.47	
Gd	9.22	8.56	8.42	6.74	7.79	8.03	3.56	3.30	7.42	8.20	6.65	6.23	4.95	5.40	6.54	6.67	6.60	
Tb	1.40	1.45	1.29	1.13	1.27	1.27	0.55	0.52	1.15	1.27	1.02	0.96	0.79	0.83	1.07	1.10	1.07	
Dy	9.42	9.64	8.05	7.64	8.24	8.16	3.53	3.28	7.70	8.25	6.58	6.18	4.90	5.33	6.86	6.84	6.91	
Ho	2.00	2.02	1.58	1.61	1.72	1.74	0.76	0.67	1.60	1.69	1.33	1.28	1.04	1.09	1.46	1.47	1.51	
Er	6.27	6.04	4.68	5.02	5.16	5.21	2.22	2.06	4.71	5.04	3.85	3.77	2.75	3.21	4.25	4.29	4.36	
Tm	0.92	0.88	0.67	0.71	0.77	0.77	0.31	0.28	0.68	0.73	0.56	0.52	0.41	0.47	0.61	0.63	0.64	
Yb	6.35	5.69	4.46	5.04	5.37	5.45	2.19	1.90	4.59	4.91	3.61	3.41	2.80	3.16	4.30	4.32	4.37	
Lu	0.96	0.87	0.66	0.76	0.83	0.82	0.33	0.31	0.73	0.72	0.56	0.52	0.42	0.47	0.62	0.66	0.64	
Hf	9.61	7.64	9.66	9.14	8.78	10.84	3.58	3.26	7.36	8.32	5.71	4.62	n.a.	4.33	6.54	6.49	6.71	
Ta	1.37	1.36	1.05	1.25	1.69	1.05	0.81	0.85	1.03	1.11	0.88	0.83	n.a.	0.76	0.67	0.75	0.76	
Pb	3.49	3.12	2.95	68.95	82.08	4.38	1.80	2.33	3.80	3.48	3.71	1.25	n.a.	1.36	7.17	3.27	2.81	
Th	5.26	5.21	6.06	5.15	5.67	4.97	2.03	1.89	3.63	4.20	2.87	1.23	n.a.	1.58	2.64	3.08	3.33	
U	1.34	1.27	1.48	1.23	1.41	0.53	0.48	0.43	0.91	1.10	0.71	0.33	n.a.	0.40	0.67	0.85	0.78	
Ti/Zr	3	3	3	3	3	6	36	36	17	17	25	38	n.a.	38	30	26	24	
Zr/Y	6.2	5.1	8.8	8.0	6.7	8.6	6.9	7.0	6.5	7.2	5.9	5.5	n.a.	5.8	6.8	6.4	6.1	

n.a. = not analyzed

Table 2. Continued.

Lithology	Basalt				Dolerite												BCR 2g (n=7)	σ	Jochum et (2011)
	FW	FW	FW	HW	FW	FW	FW	HW	FW	HW	HW	HW	HW	FW	FW				
	Jaguar	Jaguar	Jaguar	Bentley	Jaguar	Jaguar	Jaguar	Jaguar	Jaguar	Bentley	Bentley	Bentley	Bentley	Bentley	Bentley				
	JB 44675	JB 44677	JB 44696	JB 44907	JB 44667	JB 44672	JB 44673	JB 44686	JB 44703	JB 44605	JB 44643	JB 44908	JB 44912	JB Dol-01	JB Dol-02				
Sc	30.2	27.7	31.9	34.4	n.a.	50.6	55.4	50.2	52.5	44.0	50.7	41.2	52.1	61.9	53.3	35.0	0.8	33.0	
Ti	10646	9632	11730	7175	6097	11966	5589	6916	7138	7139	6735	6683	6628	7209	5930	13290	259	14100	
V	255	232	299	202	n.a.	595	306	302	329	299	286	280	317	368	312	418	8.2	425	
Cr	5.3	5.3	4.7	190.9	n.a.	12.9	157.2	28.4	30.9	16.7	26.8	15.6	50.2	220.7	190.0	14.5	0.8	17	
Mn	1956	3085	1953	1589	n.a.	2147	1609	1967	1825	1277	1236	1196	1575	2168	875	1478.4	14.6	1550	
Co	38.2	40.0	41.1	32.2	n.a.	70.9	59.0	57.0	59.2	49.6	57.8	46.5	53.8	48.1	42.0	36.8	0.8	38	
Ni	7.9	9.2	10.9	79.5	n.a.	41.7	104.3	60.2	64.4	41.3	60.8	38.7	69.5	68.7	75.5	11.6	0.8	13	
Cu	46.1	157.0	131.6	68.0	n.a.	185.6	195.3	103.2	128.9	132.0	124.9	123.6	112.2	112.9	141.0	17.7	0.9	21	
Zn	758	379	117	58	n.a.	143	88	76	200	76	77	71	86	95	355	157	3.2	125	
Rb	15.5	58.6	26.8	46.2	n.a.	36.2	1.2	2.8	42.9	3.0	0.2	2.8	0.1	117.7	41.0	49	1.2	47	
Sr	100.1	40.6	139.8	135.7	n.a.	159.5	174.1	150.2	141.4	236.1	276.0	221.0	206.0	72.2	74.8	341.4	7.3	342	
Y	40.3	42.7	42.8	26.5	21.3	39.5	20.7	29.9	28.5	29.1	28.3	27.2	27.7	23.2	15.8	32.7	0.9	35.0	
Zr	211	185	218	136	70	124	56	97	96	102	97	95	86	74	77	176	4	184	
Nb	9.9	8.6	10.1	7.9	2.9	5.1	2.4	4.1	3.9	4.3	4.1	4.0	3.7	3.0	3.1	11.9	0.3	12.5	
Cs	0.29	0.77	0.45	1.57	n.a.	16.87	0.23	0.16	7.05	1.21	0.28	1.13	0.16	3.05	1.08	1.15	0.1	1.16	
Ba	492	489	568	321	n.a.	135	22	56	338	39	30	36	8	589	469	684	15	683	
La	20.4	19.0	21.2	14.3	5.3	7.8	3.6	6.7	6.5	7.2	6.3	6.7	5.3	4.7	4.3	25.1	0.7	24.7	
Ce	47.3	43.2	48.3	32.6	13.2	19.3	9.1	16.3	15.9	17.6	15.6	16.5	13.7	11.4	10.6	52.1	0.8	53.3	
Pr	6.34	5.78	6.57	4.55	1.84	2.93	1.44	2.39	2.39	2.55	2.34	2.38	2.09	1.59	1.53	6.61	0.2	6.70	
Nd	28.1	25.9	29.1	20.2	9.4	14.9	7.4	11.8	11.7	12.3	11.7	11.5	10.7	7.4	7.6	28.0	0.8	28.9	
Sm	6.63	6.28	6.79	4.81	2.78	4.53	2.38	3.54	3.47	3.75	3.58	3.51	3.20	2.34	2.46	6.51	0.1	6.59	
Eu	1.73	3.26	1.89	1.62	0.99	1.53	0.85	1.12	1.25	1.08	1.09	1.01	1.09	0.62	0.46	1.94	0.1	1.97	
Gd	6.86	6.92	7.40	5.05	3.40	5.88	3.00	4.55	4.33	4.42	4.37	4.14	4.11	3.24	2.82	6.46	0.2	6.71	
Tb	1.13	1.12	1.15	0.75	0.59	1.01	0.53	0.77	0.75	0.78	0.74	0.73	0.72	0.59	0.46	0.98	0.0	1.02	
Dy	7.17	7.55	7.63	4.94	3.84	6.99	3.71	5.22	5.17	5.33	4.98	4.99	4.91	4.11	2.88	6.14	0.2	6.44	
Ho	1.51	1.55	1.55	0.99	0.82	1.46	0.78	1.13	1.09	1.11	1.05	1.03	1.04	0.88	0.64	1.24	0.0	1.27	
Er	4.51	4.58	4.72	2.87	2.36	4.47	2.41	3.41	3.23	3.33	3.23	3.12	3.19	2.62	1.95	3.54	0.1	3.70	
Tm	0.65	0.65	0.65	0.38	0.34	0.63	0.33	0.48	0.46	0.45	0.45	0.42	0.46	0.39	0.30	0.49	0.0	0.51	
Yb	4.19	4.48	4.41	2.68	2.46	4.26	2.21	3.19	3.14	3.11	3.06	2.91	2.97	2.73	2.19	3.23	0.1	3.39	
Lu	0.64	0.66	0.65	0.39	0.36	0.64	0.34	0.50	0.49	0.48	0.47	0.45	0.47	0.41	0.33	0.48	0.0	0.50	
Hf	5.70	4.96	5.84	3.42	n.a.	3.60	1.70	2.75	2.68	2.93	2.84	2.75	2.44	2.21	2.08	4.74	0.2	4.84	
Ta	1.06	0.62	0.74	0.53	n.a.	0.61	0.43	0.46	0.40	0.41	0.52	0.39	0.38	0.18	0.19	0.73	0.0	0.78	
Pb	6.73	3.46	3.15	3.63	n.a.	2.97	2.58	1.09	3.48	1.26	0.89	1.18	6.57	13.57	5.68	11.05	0.9	11.00	
Th	2.48	2.17	2.56	0.92	n.a.	0.66	0.31	0.73	0.64	0.73	0.61	0.69	0.52	0.42	0.55	5.86	0.2	5.90	
U	0.64	0.57	0.62	0.25	n.a.	0.15	0.07	0.19	0.15	0.19	0.17	0.18	0.12	0.12	0.14	1.68	0.0	1.69	
Ti/Zr	50	52	54	53	88	97	99	72	75	70	70	70	77	97	77				
Zr/Y	5.2	4.3	5.1	5.1	3.3	3.1	2.7	3.2	3.4	3.5	3.4	3.5	3.1	3.2	4.9				

n.a. = not analyzed

Table 3. Platinum-group element composition of the Jaguar and Bentley volcanic rocks (ppb)

Sample	Ir (ppb)	ρ	Ru (ppb)	ρ	Rh (ppb)	ρ	Pt (ppb)	ρ	Pd (ppb)	ρ	Re (ppb)	ρ	Pd/MgO $\times 10^9$	Pd/Pt
<i>Rhyolite/Dacite</i>														
JB 44699	0.005	0.0002	<0.001		0.001	0.0002	0.332	0.005	<0.008		0.01	0.00		
JB 44913	<0.0002		<0.001		<0.0003		<0.004		<0.008		<0.008			
JB 44922	<0.0002		<0.001		<0.0003		0.005	0.002	<0.008		<0.008		<0.003	<1.4
JB Dac-01	0.0002	0.0001	0.001	0.000	0.001	0.0001	0.044	0.002	0.008	0.003	0.47	0.01	0.002	0.19
<i>Andesite</i>														
JB 44663	0.014	0.0006	0.026	0.001	0.037	0.001	0.698	0.010	1.04	0.02	0.29	0.01	0.16	1.5
JB 44665	0.008	0.0002	0.046	0.002	0.036	0.0005	0.600	0.010	0.820	0.006	0.34	0.01	0.13	1.4
JB 44640	<0.0002		<0.001		<0.0003		<0.004	0.002	0.010	0.003	0.07	0.00		
JB 44904	<0.0002		<0.001		<0.0003		<0.004	0.002	<0.008		0.12	0.01		
JB 44906	<0.0002		<0.001		<0.0003		<0.004	0.002	<0.008		0.93	0.01		
JB 44613	0.012	0.0003	0.024	0.002	0.058	0.002	0.783	0.020	1.25	0.03	0.83	0.02	0.24	1.6
JB 44616	0.011	0.0007	0.014	0.001	0.057	0.001	0.759	0.006	1.12	0.01	0.70	0.01		
JB 44619	0.012	0.0004	0.027	0.001	0.065	0.001	0.800	0.018	1.14	0.03	0.53	0.02	0.20	1.5
JB And-01	0.000	0.0001	0.002	0.001	0.001	0.0001	0.011	0.002	0.003	0.003	0.00	0.00	0.006	0.72
JB And-02	0.005	0.0001	0.012	0.001	0.012	0.0004	0.359	0.005	0.052	0.004	0.32	0.01	0.018	0.14
JB And-03	0.004	0.0003	0.004	0.001	0.008	0.0003	0.274	0.008	0.058	0.004	0.20	0.01	0.021	0.21
<i>Basalt</i>														
JB 44677	<0.0002		<0.001		<0.0003		0.003	0.002	<0.008		0.87	0.01		
JB 44696	<0.0002		<0.001		<0.0003		0.012	0.002	<0.008		1.11	0.02	<0.003	<0.65
JB 44907	0.010	0.0003	0.021	0.001	0.014	0.0005	0.476	0.005	0.083	0.004	0.56	0.01	0.033	0.17
<i>Dolerite</i>														
JB 44667	0.101	0.0021	0.028	0.002	0.310	0.007	8.27	0.192	5.029	0.074	1.11	0.03		
JB 44672	<0.0002		<0.001		<0.0003		<0.004		<0.008		1.68	0.02		
JB 44673	0.050	0.0012	0.018	0.001	0.065	0.001	5.78	0.061	1.92	0.02	1.10	0.01	0.24	0.3
JB 44605	0.013	0.0005	0.002	0.001	0.028	0.001	1.82	0.029	0.55	0.01	1.76	0.02	0.08	0.3
JB Dol-02	0.124	0.0011	0.034	0.001	0.630	0.009	9.76	0.109	12.5	0.2	0.29	0.01	3.50	1.3
<i>TDB-1 (CANMET dolerite reference material)</i>														
#1	0.098	0.001	0.183	0.005	0.445	0.003	4.99	0.02	22.1	0.2	0.729	0.006		
#2	0.070	0.001	0.161	0.003	0.417	0.003	4.25	0.02	22.3	0.2	0.721	0.007		
#3	0.071	0.003	0.175	0.008	0.427	0.012	4.42	0.15	22.2	0.6	0.717	0.023		
Average (n=3)	0.079		0.173		0.429		4.55		22.2		0.722			
M&M ^a (n=7)	0.075	0.009	0.198	0.008	0.471	0.039	5.01	0.17	24.3	1.7	0.790	0.020		
P ^b (n=8)	0.078	0.003					4.40	0.15	24.8	0.7				
Certified ^c	0.150		0.300		0.700		5.80		22.4					

^a Meisel and Moser (2004), high pressure asher (HPA) digestion ID-ICP-MS.^b Peucker-Ehrenbrink et al. (2003), Ni-sulfide fire assay ID-ICP-MS.^c Govindaraju (2007), Note that Ir, Ru and Rh values are provisional values

Figure 1

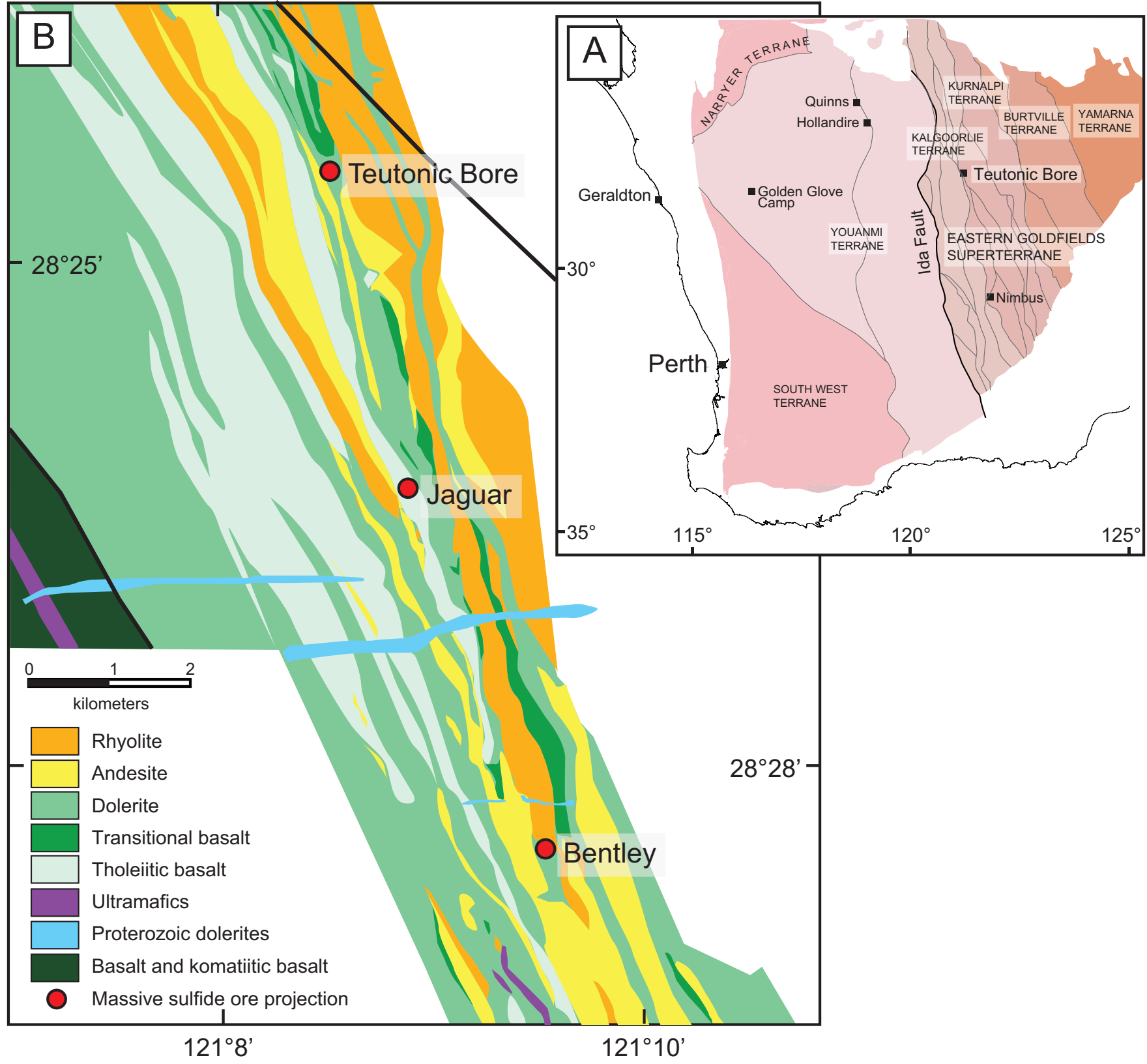


Figure 2

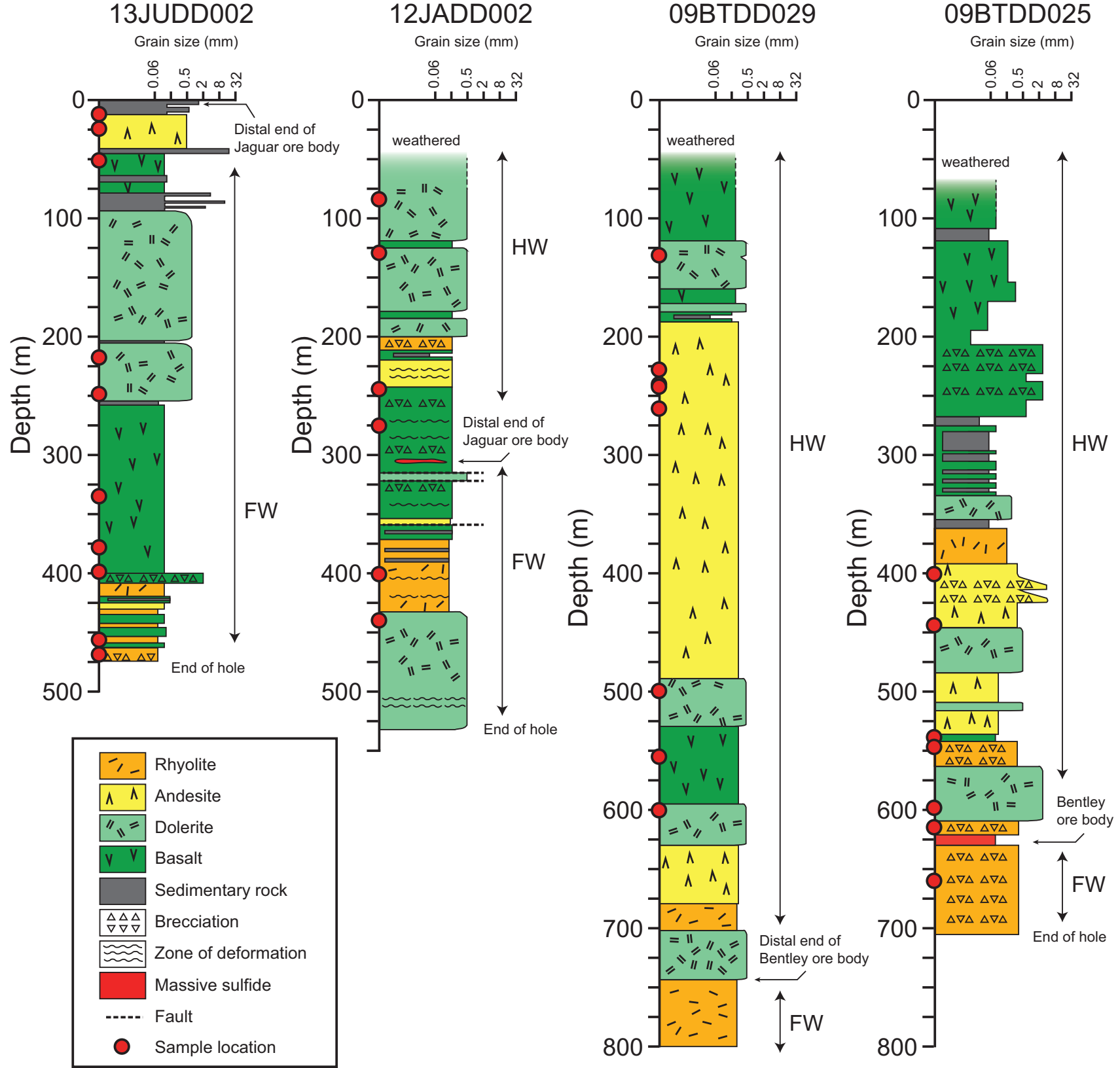


Figure 3

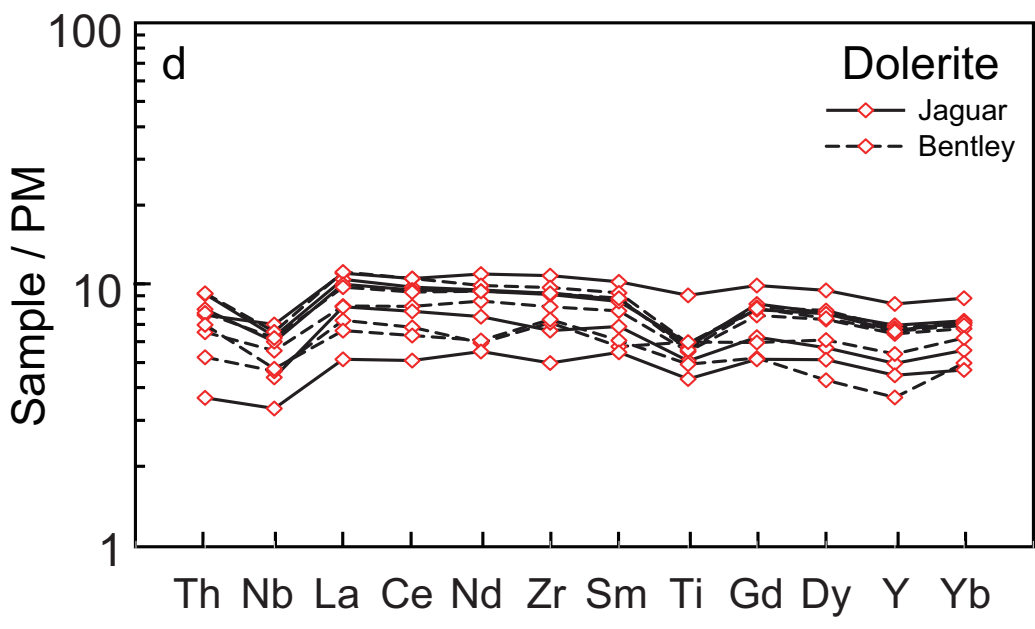
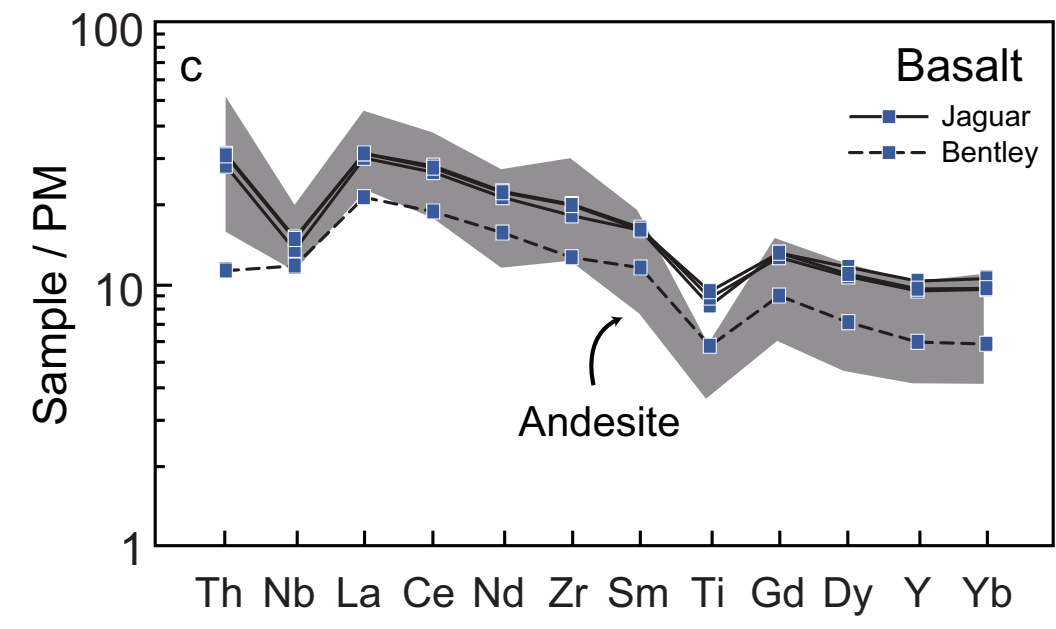
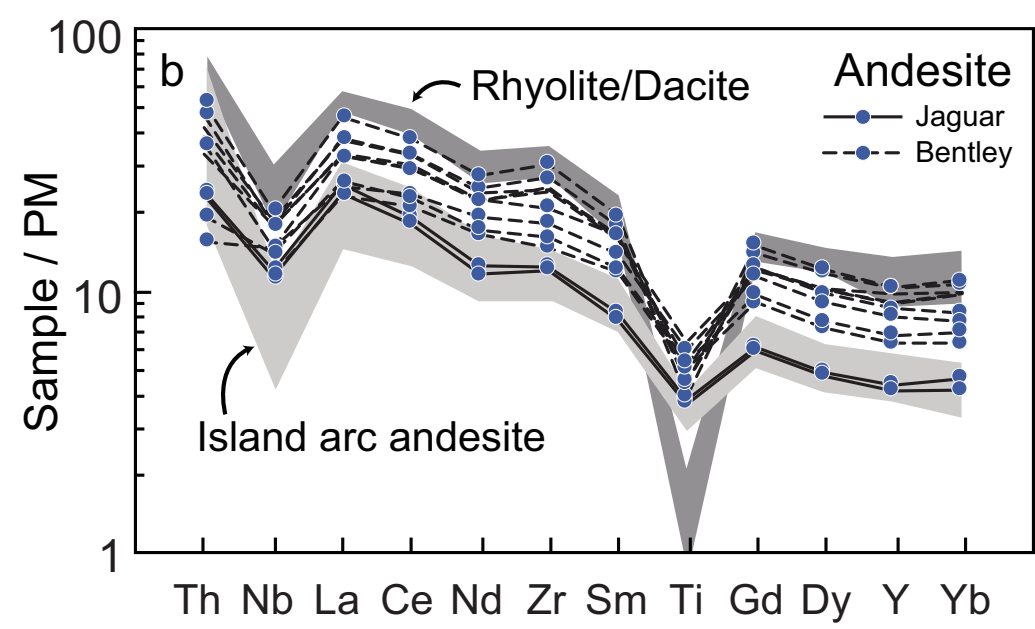
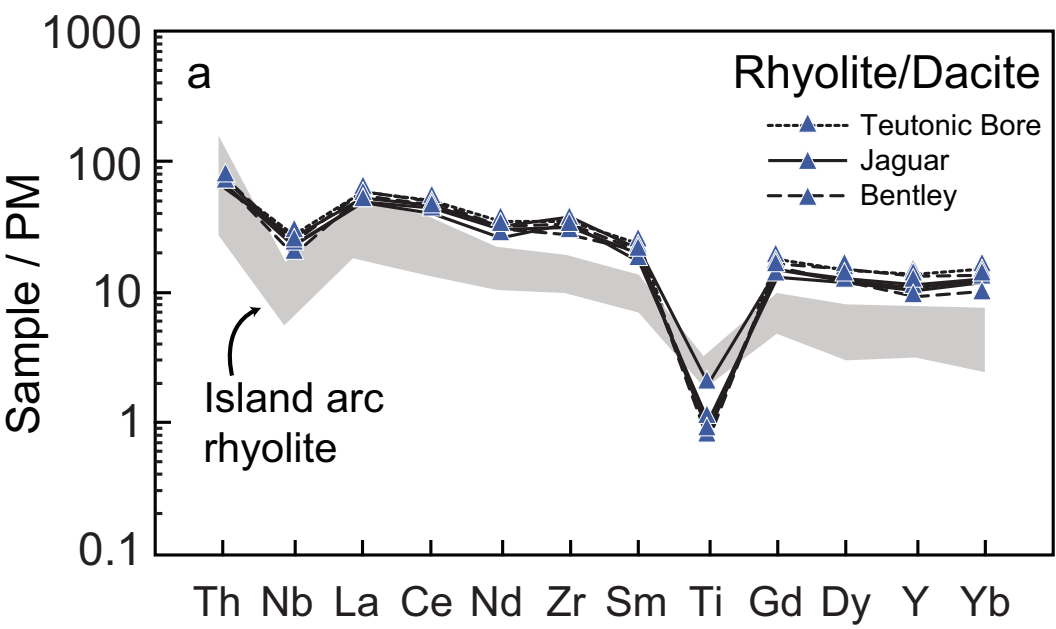


Figure 4

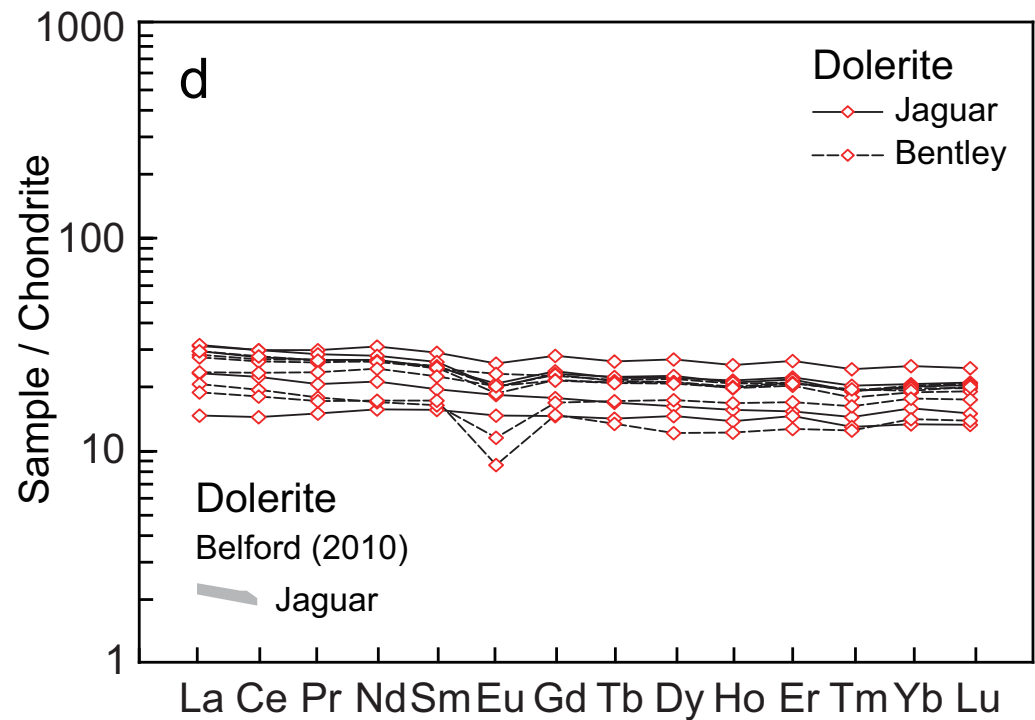
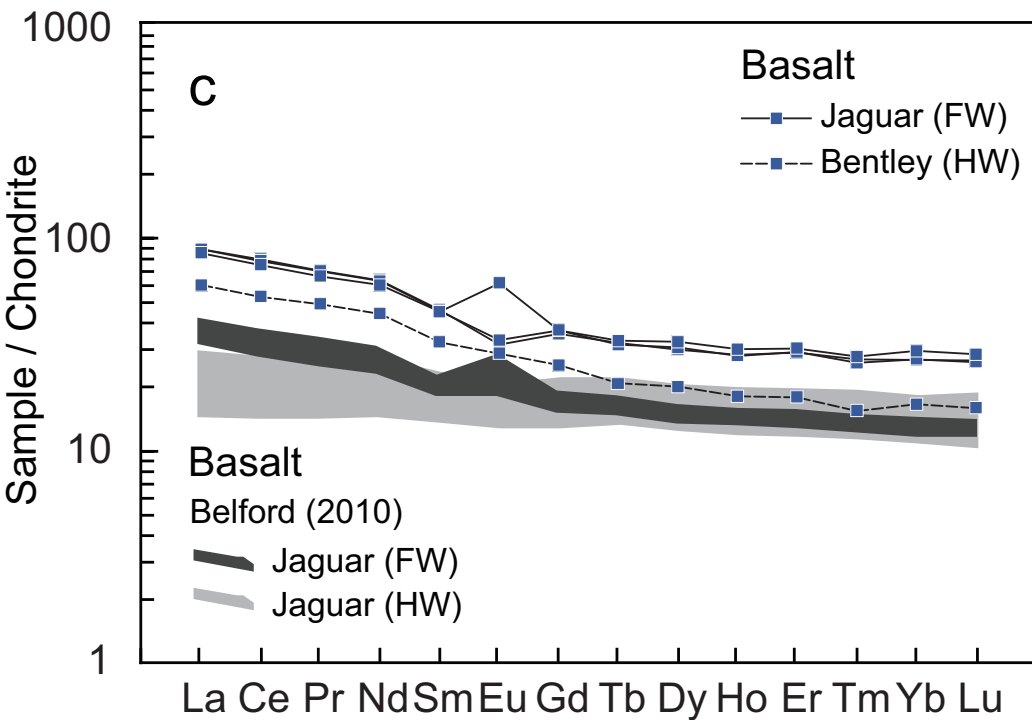
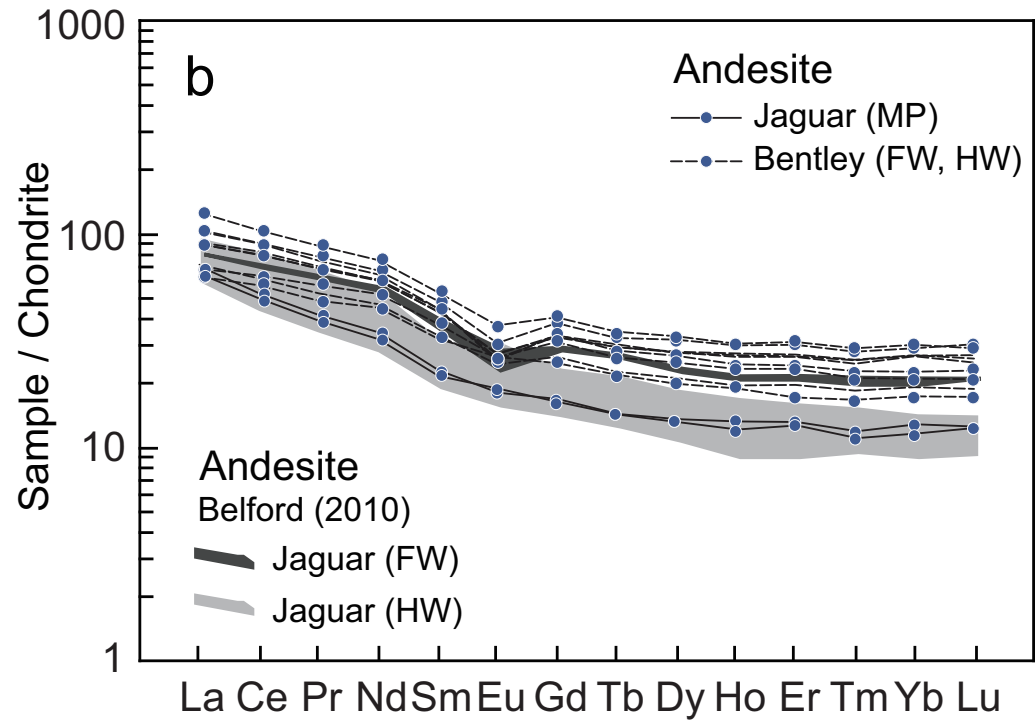
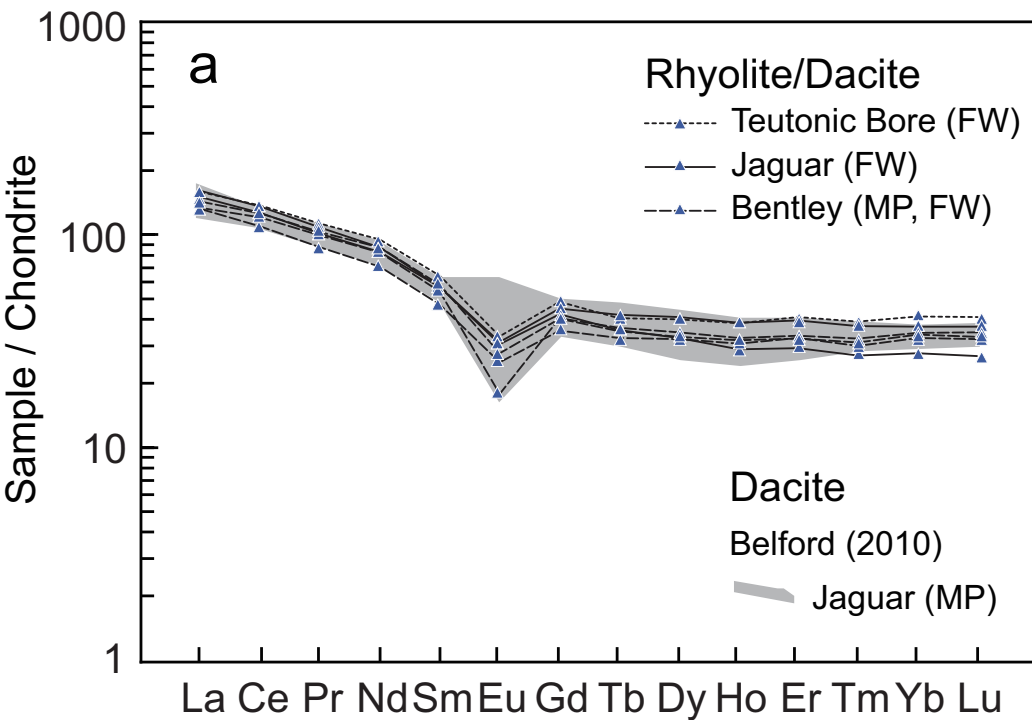


Figure 5

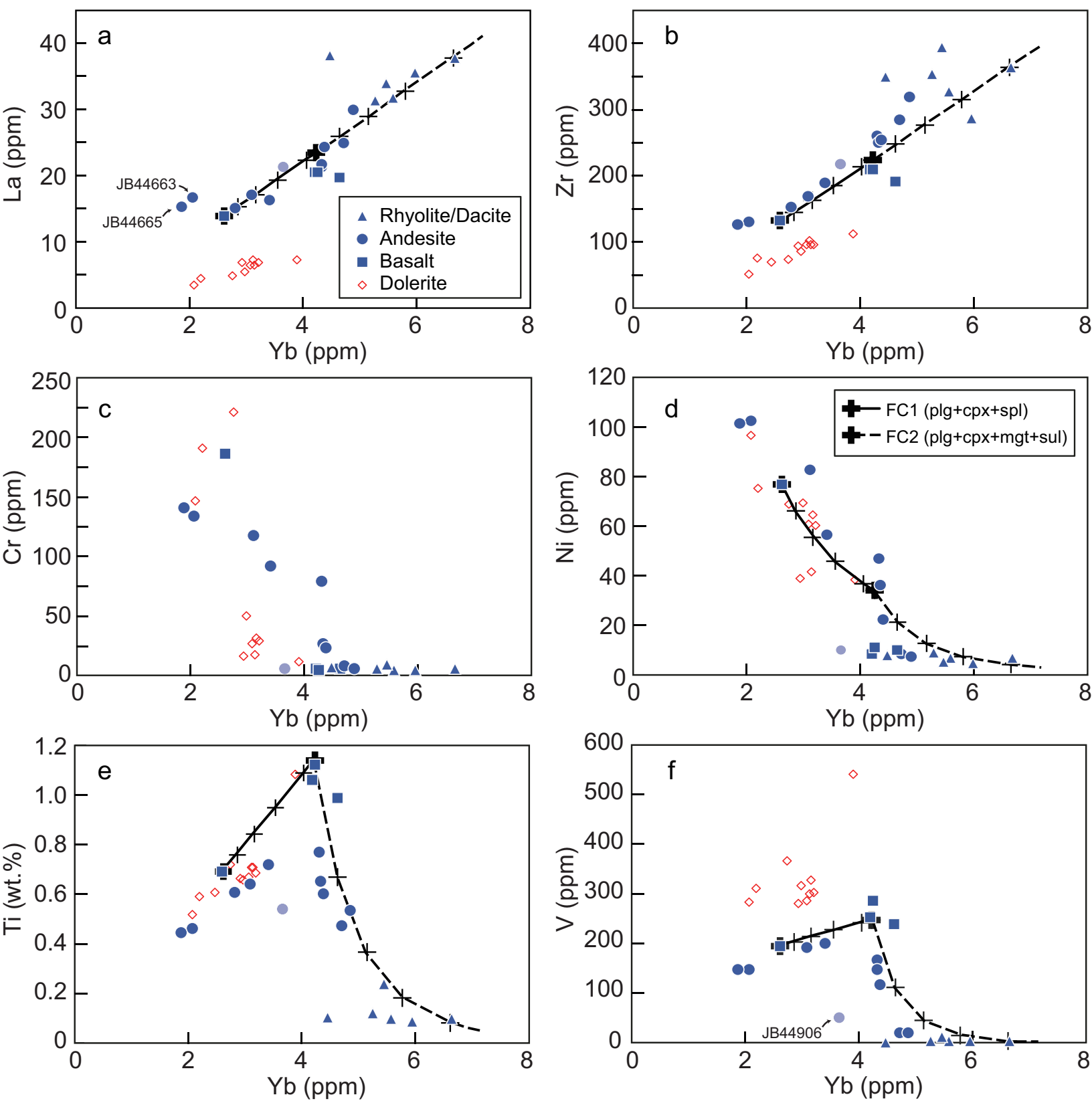


Figure 6

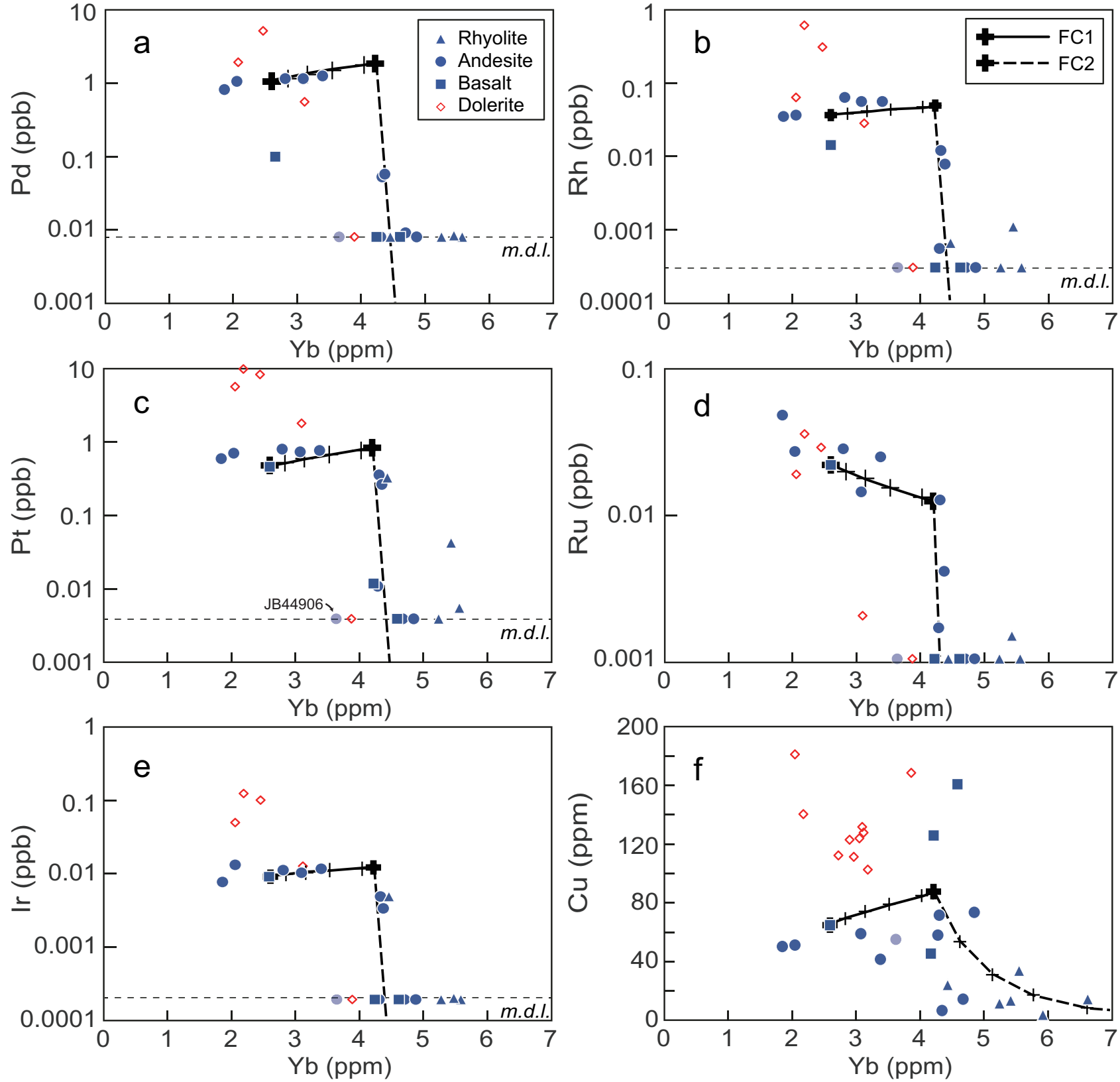


Figure 7

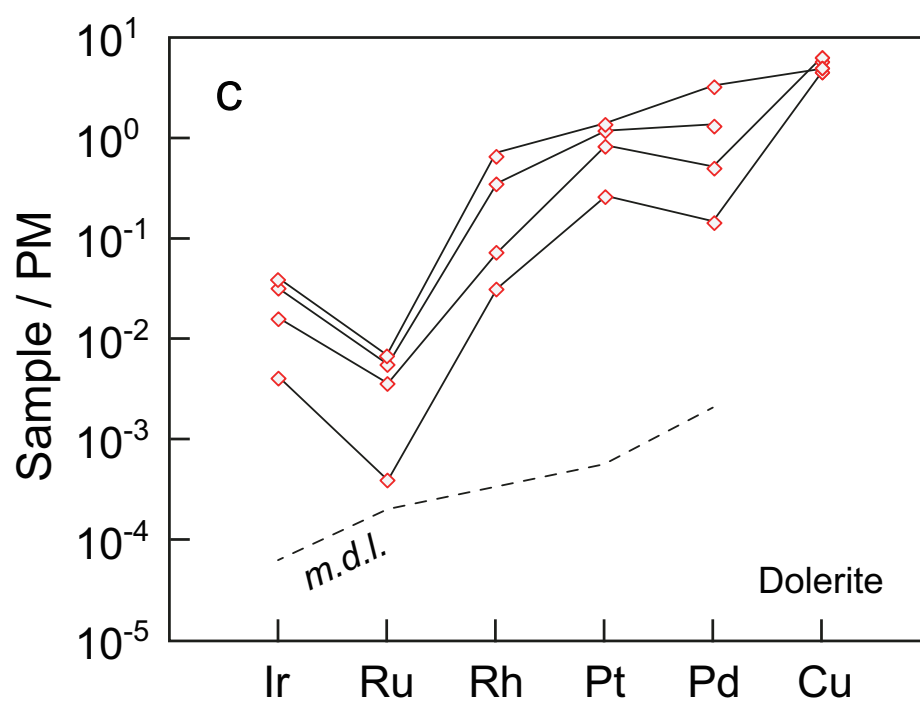
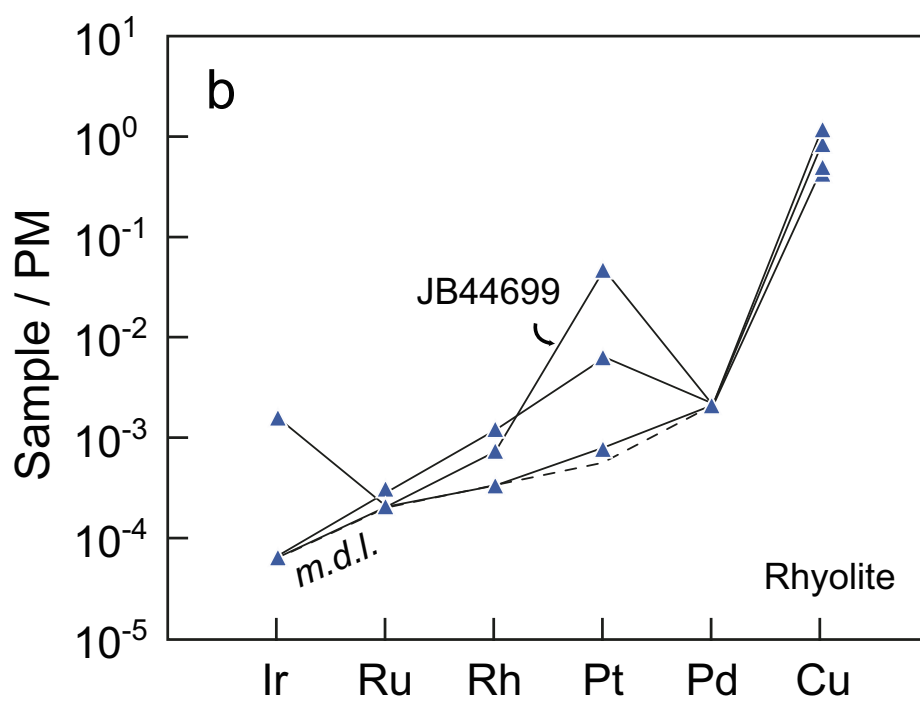
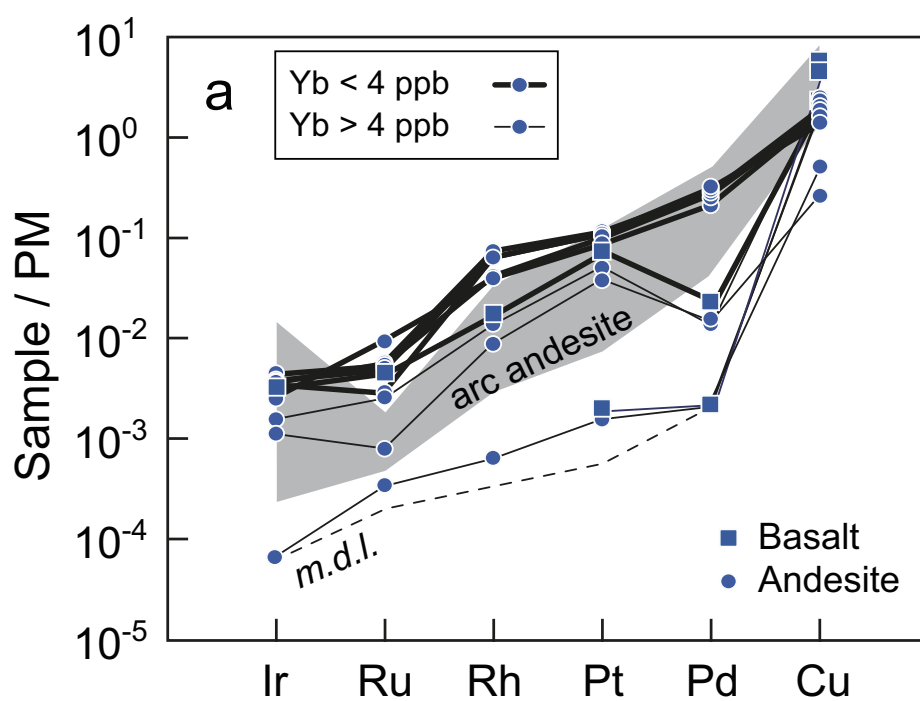


Figure 8

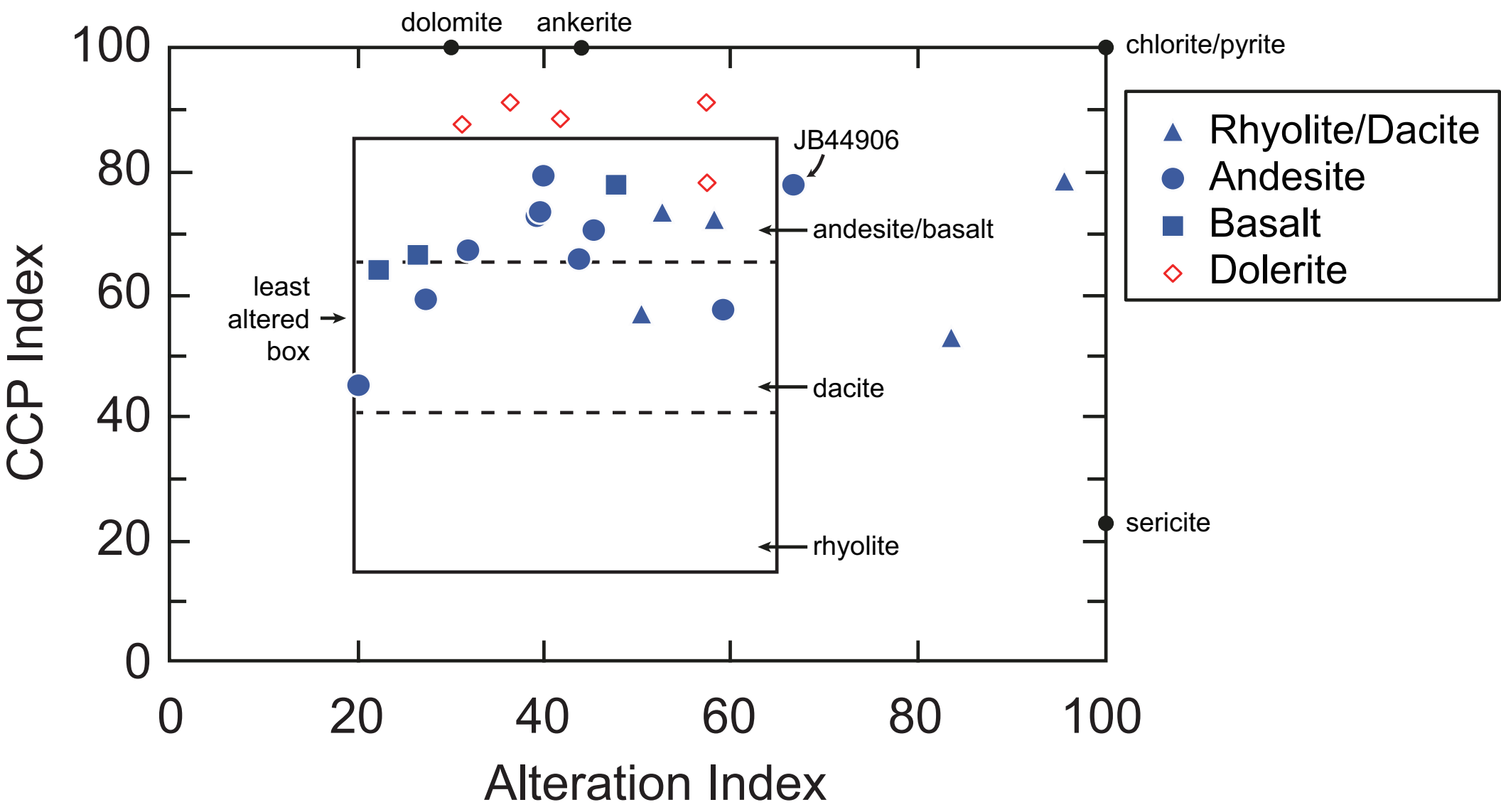


Figure 9

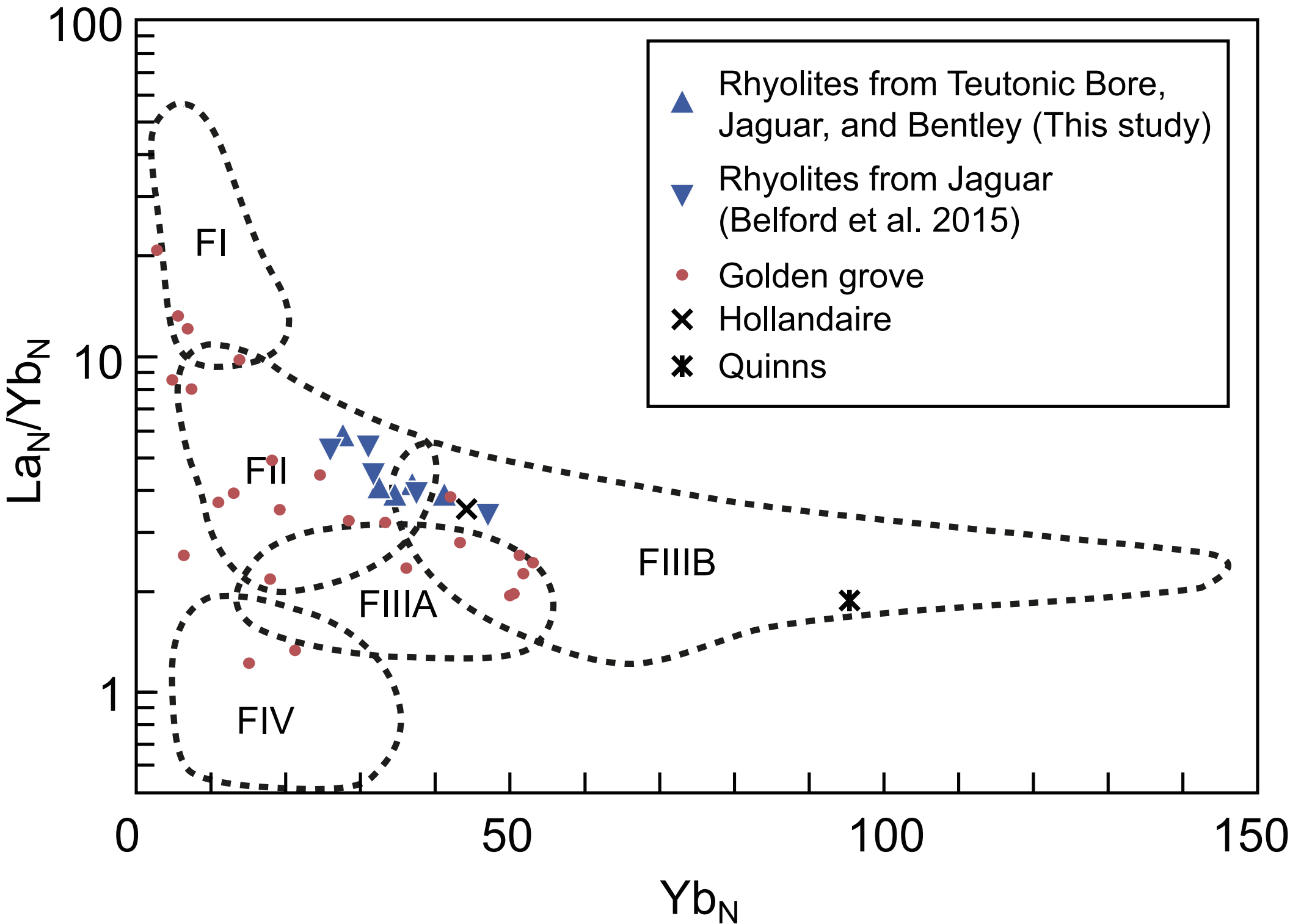


Figure 10

